INVESTIGATION OF A TWO-DIMENSIONAL THEORY TO PREDICT ASCENDING MOTION AT THE TOP OF THE PLANETARY BOUNDARY LAYER IN THE TROPICS

by

PETER JOHN SOUSOUNIS
B.S. Physics, Drexel University
(1983)

SUBMITTED TO THE
DEPARTMENT OF EARTH, ATMOSPHERIC, AND PLANETARY SCIENCES
IN PARTIAL FULFILLMENT OF THE REQUIREMENTS
FOR THE DEGREE OF
MASTER OF SCIENCE IN METEOROLOGY

at the

MASSACHUSETTS INSTITUTE OF TECHNOLOGY
December 1986

Signature of Author . . . . . .
Department of Earth, Atmospheric, and Planetary Sciences
December1986

Certified by . . . . . .
Professor Kerry A. Emanuel
Thesis Supervisor

Certified by . . . . . .
Professor Peter H. Stone
Thesis Supervisor

Accepted by . . . . . .
William F. Brace
Chairman, Department of Earth, Atmospheric, and Planetary Sciences

INVESTIGATION OF A TWO-DIMENSIONAL THEORY TO PREDICT ASCENDING MOTION AT THE TOP OF THE PLANETARY BOUNDARY LAYER IN THE TROPICS

by

PETER JOHN SOUSOUNIS

Submitted to the
Department of Earth, Atmospheric, and Planetary Sciences
on December 17, 1986 in partial fulfillment of the
requirements for the Degree of Master of Science in Meteorology

ABSTRACT

A two-dimensional theory is presented to explain the relationship between sea surface temperature (SST) distribution and the resulting vorticity and vertical motions at the top of the planetary boundary layer (PBL) in the tropics. The assumptions and predictions of the theoretical model are investigated using data sets from various two-dimensional General Circulation Model (2-D GCM) runs and also using a real, three-dimensional (3-D) data set. The results are then evaluated to determine the feasibility of applying the model. Three major assumptions of the model which are investigated are: (1) that saturated moist entropy (S^*) and a quantity analogous to absolute angular momentum (M) are conserved by ascending parcels above the top of the PBL; (2) that the vertical velocity at the top of the PBL is proportional to the vorticity at that level (Ekman approximation); and (3) that the meridional temperature gradient at the top of the PBL is equal to that at the sea surface. The two major predictions of the model are: (1) that the vertical component of the relative vorticity at the top of the PBL is proportional to the meridional gradient of the saturated moist entropy at that level and (2) that the maximum upward velocity at the top of the PBL is equatorward of a minimum (maximum) in the meridional sea surface temperature (SST) gradient in the northern (southern) hemisphere.

The various 2-D model runs differ from one another in their parameterizations of moist convection, specifications of large-scale eddy forcing and momentum mixing, and SST distributions. Assumption (1) is verified by those runs where no momentum mixing was allowed, assumption (2) is qualitatively verified by some runs even near the equator where Ekman balance tends to be a poor assumption, and assumption (3) is verified by all runs. Prediction (1) is only marginally verified by those runs where no momentum mixing was allowed, while prediction (2) is qualitatively verified by those runs which showed a strong, double Inter-Tropical Convergence Zone (ITCZ).

With respect to the real data set, regions for times of year when the thermodynamic structure was quasi-two-dimensional and meridionally symmetric, as well as other cases, were studied. Assumption (1) is not verified by any of the selected cases, assumption (2) is qualitatively verified by those cases which had relatively strong vertical velocities, and assumption (3) again is verified by all of the selected cases. Predictions (1) and (2) are not verified by any of the selected cases.

For the 2-D data set it is concluded that lack of verification of predictions (1) and (2) are a result of both M and S^* not being conserved quantities along streamlines in the rising branch of the Hadley Circulation. For the 3-D data set it is concluded that lack of verification of predictions (1) and (2) are a result of S^* and M not being congruent. Limitations in the data set prevent further determination of the degrees of non-conservation of either quantity. Hence the theory as presented here may not be used to account for the vertical velocity patterns at the top of the PBL in the tropics. Furthermore, any valid attempt to explain phenomena in this region must account for the non-conservation of absolute angular momentum and possibly saturated moist entropy.

Kerry A. Emanuel and Peter H. Stone
Thesis supervisors

TABLE OF CONTENTS

ABSTRACT 2

ACKNOWLEDGEMENTS 5

CHAPTER 1: INTRODUCTION 6

CHAPTER 2: THEORETICAL CONSIDERATIONS 9

CHAPTER 3: TWO-DIMENSIONAL DATA ANALYSIS 19

3.1 Data Description 19

3.2 Computation of M and S^* Fields 22

3.3 Analysis of M, AM, S^*, and Φ Fields 25

3.4 Ekman Velocity Assumption 40

3.5 Meridional Temperature Gradients 46

3.6 Theoretical Vorticity 48

3.7 Vertical Velocity and Sea Surface Temperature . . 62

CHAPTER 4: THREE-DIMENSIONAL DATA ANALYSIS 65

4.1 Data Description 65

4.2 Selection of Regions 65

4.3 Analysis of S^* and M Fields 67

4.4 Ekman Velocity Assumption 73

4.5 Meridional Temperature Gradients 79

4.6 Theoretical Vorticity 82

4.7 Vertical Velocity and Sea Surface Temperature . . 85

CHAPTER 5: SUMMARY AND CONCLUSIONS 91

ILLUSTRATION LIST 98

REFERENCES 101

ACKNOWLEDGEMENTS

First, I would like to thank Kerry Emanuel, one of my thesis advisors, for suggesting this topic for research and for alloting me periods of his valuable time for discussions whose content served to enlighten my knowledge of the thermodynamics of the tropical atmosphere. I would also like to thank Peter Stone, my other thesis advisor, for providing the two-dimensional data sets used for the analyses and also for some of his valuable time during which elucidating explanations of the various model parameterizations were provided. Next, I would like to extend my appreciation to Rick Rosen of AER in Cambridge, MA for providing the magnetic tape containing the Oort data set; and to Mark Handel, one of my two officemates, for proofreading the initial draft and providing comments and suggestions for improvement. Of course, I would also like to thank Kuan-man Xu, my other officemate, as well as all my other friends at CMPO, whose humor and companionship provided for a delightful environment in which to work. Finally and most importantly, I would like to give special thanks to my fiancée Maria, whose continuous moral support, love, and devotion during this period proved a most valuable source of motivation as well as inspiration - thanks hun!

CHAPTER I

INTRODUCTION

Various general circulation models (GCM's) have attempted to simulate the Hadley Circulation. Two-dimensional (2-D) models are thought to be particularly useful for studying the effects of different parameterizations and boundary conditions on the zonally averaged flow. The reason for this is that such models can incorporate interactions between latitudinal and vertical structure that one-dimensional (1-D) models cannot and at the same time, are more efficient computationally than three-dimensional (3-D) GCM's. There is lack of agreement, however, in some of the modeled features amongst 2-D GCM's. One feature in particular is the latitudinal variation of vertical motions near the equator. While some models show only one distinct area of rising motion (a single Inter-Tropical Convergence Zone (ITCZ)), other models show two distinct regions of rising motion. One such model whose output yields one ITCZ is the Goddard Laboratory for Atmospheric Sciences (GLAS) GCM. In these model results, the maximum vertical velocity overlies the maximum sea-surface temperature (SST) (Goswami et al., 1984). When the SST distribution was changed abruptly, so that the maximum was at another latitude, the vertical velocity maximum decayed over the old SST maximum, while a new one grew over the new SST maximum. A model which exhibits two ITCZ's is the recently developed 2-D GCM at the Goddard Institute for Space Studies (GISS). In runs having symmetric SST distributions with a single maximum at the equator, two ITCZ's

existed simultaneously on either side of the maximum. The Earth's atmosphere is much harder to categorize in this respect. At different times of the year and in various regions, the ITCZ structure has been observed as single and sometimes as double. Hence, it is difficult to ascertain which models are producing an accurate simulation and which physical processes are involved.

This paper presents a simple theory which would explain the existence of a double ITCZ . The assumptions and predictions of the theory are investigated using data from various 2-D GCM runs as well as actual, 3-D data. The results are then evaluated to determine where and how the model may be applied to explain vertical velocities at the top of the planetary boundary layer (PBL). Section II presents the theory, as well as its assumptions, predictions, and utilities. The three major assumptions of the model are: (1) that saturated moist entropy (S^*) and a quantity analogous to absolute angular momentum (M) are conserved by ascending parcels above the top of the PBL; (2) that the vertical velocity at the top of the PBL is proportional to the vorticity at that level (Ekman approximation); and (3) that the meridional temperature gradient at the top of the PBL is equal to that at the sea surface. The two major predictions of the model are: (1) that the vertical component of the relative vorticity at the top of the PBL is proportional to the meridional gradient of the saturated moist entropy at that level and (2) that the maximum upward velocity at the top of the PBL is equatorward of a minimum (maximum) in the meridional sea surface temperature (SST) gradient in the northern (southern) hemisphere. Section III contains the analysis of data

from the GISS 2-D GCM runs. The assumptions and predictions of the model are investigated by comparing theoretical calculations with actual model data. Section IV utilizes similar procedures to investigate actual 3-D data obtained from the Oort analyses. Since the theory is two-dimensional, the 3-D data was quasi-zonally averaged over certain regions of the globe found suitable for investigation. Section V contains the summary and conclusions.

CHAPTER II

THEORETICAL CONSIDERATIONS

The following has been suggested by Emanuel (personal communication, 1986). Consider the ascending branch of the Hadley Circulation to be a two dimensional moist adiabatic, non-dissipative region in steady state. Above the boundary layer, saturated moist static entropy and absolute angular momentum will thus be conserved along streamlines. Furthermore, assume the Beta-plane approximation to be valid within this region. The zonal momentum equation can thus be written as :

$$\frac{du}{dt} = \beta y v \qquad (1)$$

where u = zonal velocity,

v = meridional velocity,

β = meridional gradient of Coriolis parameter, f,

y = latitudinal distance from equator.

Hence M defined by

$$M = u - \frac{1}{2}\beta y^2 \qquad (2)$$

is conserved in the region. This quantity is analogous to absolute angular momentum (distinguished as AM in this paper). Assuming

that the zonal wind is in geostrophic balance, and that hydrostatic balance is maintained, the following can be written:

$$\beta y\, u = -g\left(\frac{\partial z}{\partial y}\right)_P \tag{3}$$

$$\alpha = -g\left(\frac{\partial z}{\partial P}\right)_y \quad . \tag{4}$$

The thermal wind relationship is thus :

$$\beta y\left(\frac{\partial u}{\partial P}\right)_y = \left(\frac{\partial \alpha}{\partial y}\right)_P \quad . \tag{5}$$

Using the expression for M, the above can be rewritten as

$$\beta y\left(\frac{\partial M}{\partial P}\right)_y = \left(\frac{\partial \alpha}{\partial y}\right)_P \quad . \tag{6}$$

The RHS of Eq. (6) can be rewritten to give :

$$\beta y\left(\frac{\partial M}{\partial P}\right)_y = \left(\frac{\partial \alpha}{\partial S^*}\right)_P \left(\frac{\partial S^*}{\partial y}\right)_P \quad , \tag{7}$$

where S^* is the saturated moist entropy. From Maxwell's relations,

$$\left(\frac{\partial \alpha}{\partial S^*}\right)_P = \left(\frac{\partial T}{\partial P}\right)_{S^*} \quad . \tag{8}$$

And thus Eq. (7) becomes :

$$\beta y\left(\frac{\partial M}{\partial P}\right)_y = \left(\frac{\partial T}{\partial P}\right)_{S^*}\left(\frac{\partial S^*}{\partial y}\right)_P . \qquad (9)$$

Now, if it may be assumed that S^* and M are conserved along streamlines, then S^* may be written as a function of M :

$$S^* = S^*(M) \qquad (10)$$

and Eq. (9) becomes :

$$\beta y\left(\frac{\partial M}{\partial P}\right)_y = \left(\frac{\partial T}{\partial P}\right)_{S^*}\left(\frac{dS^*}{dM}\right)\left(\frac{\partial M}{\partial y}\right)_P \qquad \text{or,} \qquad (11)$$

$$\beta y\left(\frac{\partial y}{\partial P}\right)_M = -\left(\frac{dS^*}{dM}\right)\left(\frac{\partial T}{\partial P}\right)_{S^*} . \qquad (12)$$

Equation (12) states that, given a constant dS^*/dM along streamlines (shown to be nearly the case later on) for a given region, moving upward at a fixed latitude, lines of constant S^* and M will be flared more outward with height since $|\partial T/\partial P|_{S^*}$ increases with decreasing temperature. Alternatively, these isentropes (constant S^* lines) and constant M-lines will become less flared when moving poleward along lines of constant pressure. Integrating Eq. (12) along constant M-lines yields an expression for

the shape of the lines :

$$-\frac{1}{2}\beta y^2 = T\left(\frac{dS^*}{dM}\right) + C(M) \ , \qquad (13)$$

where C(M) is a function of M (or S^*). A more precise way of determining C would be to match Eq. (13) to a solution for the descending branch at y_0, the latitude at which the large-scale vertical velocity changes from upward to downward. If, however, $T(y_0)$ is known as a function of S^*, then C can be determined and Eq. (13) can be rewritten as :

$$\frac{1}{2}\beta(y_o^2 - y^2) = \left(\frac{dS^*}{dM}\right)(T(y) - T(y_o)) \ . \qquad (14)$$

Since dS^*/dM is a constant for a given value of S^*, its value may be looked upon as the ratio of a parcel's change in zonal velocity to its change in temperature as it travels from y to y_0 along a streamline. And now, differentiating Eq. (2) with respect to y and combining it with Eq. (14) yields an expression for the vorticity in an axially symmetric flow:

$$\frac{du}{dy} = \beta y + 2\left(\frac{\partial S^*}{\partial y}\right)\left(\frac{T(y) - T(y_o)}{\beta(y_o^2 - y^2)}\right) \ . \qquad (15)$$

This expression can be used at the top of the boundary layer to solve for du/dy at a given latitude (y).

If it may be assumed a priori (it will be shown later) that $(T(y) - T(y_0))/(\beta(y_0^2 - y^2))$ is a constant so that the second term on the RHS of Eq. (15) is only a function of $\partial S^*/\partial y$, and it is further assumed that S^* varies sinusoidally with latitude, then it can be seen that for the northern (southern) hemisphere the vorticity maximum (minimum) should occur on the equatorward side of the minimum (maximum) in $(\partial S^*/\partial y)$ within the rising region. This may be seen more intuitively by considering the following. Figure 2.1a is a latitude-pressure cross section of an S^* profile with a maximum at the equator, decreasing nonuniformly away from it with latitude. The contour interval is the same throughout. Since it has been assumed that rising parcels conserve S^* and M, the isentropes, constant M-lines, and streamlines are all congruent to one another. In order to isolate the effects of $\partial S^*/\partial y$ on the vorticity, β will for the moment be ignored. First, consider parcel A shown in figure 2.1a as it rises along streamline a. When it reaches y', it will be in a region of relatively weak meridional temperature gradient. Hence, from thermal wind considerations, the westerly wind shear is weak, and since parcels are constrained to conserve their absolute angular momentum, parcel A must have left the top of the boundary layer with relatively weak (although positive) vorticity.

Now consider parcel B, rising along streamline b. When it reaches y', it will be in a region of relatively strong meridional temperature gradient, and so by thermal wind considerations, must be in a region of relatively strong westerly wind shear. Hence, it must have left the top of the planetary boundary layer with

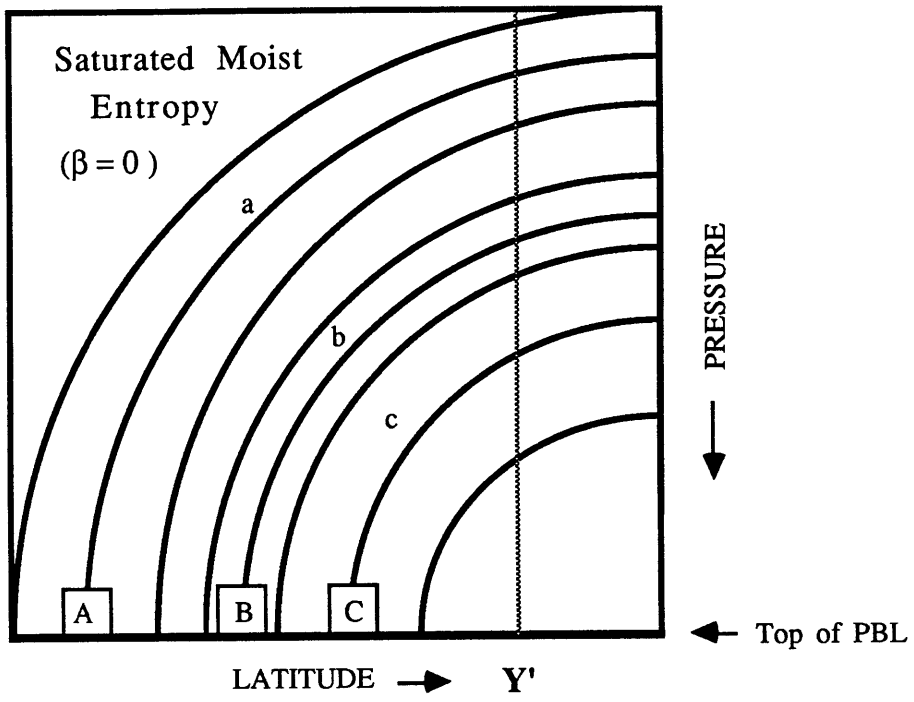

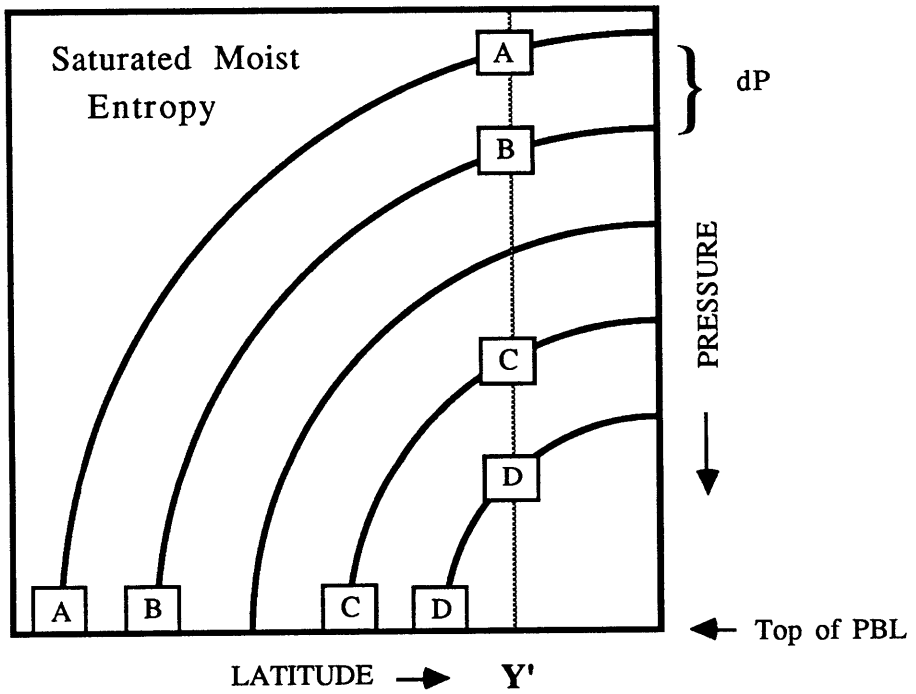

Figure 2.1 (a) contour plot showing lines of constant S^*. Streamlines and constant M lines are parallel to these. Spacing indicates weak baroclinity at streamlines a and c and strong baroclinity at streamline b. (b) Similar to (a) except for presence of β and constant spacing of contour intervals of S^*.

relatively strong positive vorticity.

Lastly consider parcel C which after rising along streamline c to y', will find itself in a region of weak meridional temperature gradient. By similar reasoning, it must have left the top of the planetary boundary layer with weak positive vorticity. Thus, it can be seen that, in the absence of β, maximum cyclonic vorticity at the top of the boundary layer will exist in a region of maximum $|dS^*/dy|$.

In order to illustrate the effect that β has in Eq. (15), consider now figure 2.1b, where dS^*/dy is constant along the top of the boundary layer. Consider first, four parcels at the top of the boundary layer at y_A, y_B, y_C, and y_D, where $y_D > y_C > y_B > y_A$. The M-values (M_i) of the parcels are :

$$M_i = u_i - \frac{1}{2}\beta y_i^2 \qquad\qquad i = A, B, C, D .$$

As the parcels rise up and cross y', they must obey the thermal wind relationship. Since y' is now a region of constant meridional temperature gradient with height, the vertical wind shear should be constant with height as well. Or, in terms of parcels,

$$\frac{\partial u_{AB}}{\partial P} = \frac{\partial u_{CD}}{\partial P}$$

where

$$\frac{\partial u_{AB}}{\partial P} = \frac{u_{ZA} - u_{ZB}}{\Delta P_{AB}}$$

u_{ZA} = u at y' along streamline A

u_{ZB} = u at y' along streamline B

ΔP_{AB} = pressure difference at y' from streamline A to B.

Since y' is constant with height, the above can be written as

$$\frac{M_A - M_B}{\Delta P_{AB}} = \frac{M_C - M_D}{\Delta P_{CD}} \quad .$$

For convenience, let $\Delta P_{AB} = \Delta P_{CD}$, $y_B = y_A + \Delta y$, and $y_D = y_C + \Delta y$. Expanding the above gives

$$u_A - u_B - \frac{1}{2}\beta\{y_A^2 - (y_A + \Delta y)^2\} =$$
$$u_C - u_D - \frac{1}{2}\beta\{y_C^2 + (y_C + \Delta y)^2\}.$$

Expanding and keeping only the terms linear in Δy leaves

$$u_A - u_B + \beta y_A \Delta y = u_C - u_D + \beta y_C \Delta y \qquad \text{or,}$$
$$\beta y_A - \frac{u_B - u_A}{\Delta y} = \beta y_C - \frac{u_D - u_C}{\Delta y} \quad .$$

Since $y_C > y_A$,

$$\frac{u_D - u_C}{\Delta y} > \frac{u_B - u_A}{\Delta y}.$$

Thus, parcels more poleward have less cyclonic vorticity than parcels more equatorward. In fact,

$$\frac{\partial}{\partial y}\left\{\frac{\partial u}{\partial y}\right\} = \beta.$$

The net result of these two effects will be a maximum (minimum) in cyclonic vorticity equatorward of a local minimum (maximum) in $(\partial S^*/\partial y)$ in the northern (southern) hemisphere.

Now, using Ekman pumping theory, the vertical velocity can be estimated at the top of the boundary layer by

$$w_E = -\left(\frac{du}{dy}\right)\frac{|f|}{f}\sqrt{\frac{K}{2|f|}} \qquad (16)$$

where f is the Coriolis parameter and K is an empirical eddy diffusion coefficient.

Lastly, if it is assumed that the temperature gradient at the top of the boundary layer is equal to that at the surface :

$$\left(\frac{dT}{dy}\right)_{PBT} = \left(\frac{dT}{dy}\right)_{SFC}, \qquad (17)$$

then the combined interpretation of Eqs. (15) - (17) is that a maximum in the vertical velocity at the top of the PBL should occur equatorward of a maximum (minimum) in meridional SST gradient in the northern (southern) hemisphere (provided K in Eq. (16) is

constant with latitude) :

$$w_E = -\left\{ \beta y + 2\frac{dS^*}{dT_S}\frac{dT_S}{dy}\left(\frac{T(y) - T(y_o)}{\beta(y_o^2 - y^2)}\right)\right\}\frac{|f|}{f}\sqrt{\frac{K}{2|f|}} \qquad (18)$$

where T_s is the surface temperature and all other variables are as previously defined.

CHAPTER III

TWO-DIMENSIONAL DATA ANALYSIS

3.1 Data Description

The data used for the analysis in this section was obtained from six different numerical experiments using a 2-D GCM at GISS. The lower boundary in the model was all ocean. For a complete description of the model, the reader should refer to Yao and Stone, 1987. These particular experiments were selected for investigation to determine the degree of validity required by each of the model assumptions in order for the model predictions to be verified. Hence, the six experiments differed from one another in the inclusion of large-scale eddy forcing, parameterization of moist convection, and degree of meridional symmetry during a particular experiment. One moist convection scheme which was used constrained a specified fraction of an entire layer of air to mix if it were unstable. A lower layer of air was either all stable or unstable. If it were all unstable, then 50% of the layer participated in the mixing process. This parameterization is referred to as C2. Another parameterization scheme which was used was one which allowed for fractions of air layers to be unstable, i.e. the entire layer did not have the same temperature. Only that portion that became unstable would participate in the mixing process. This scheme was very similar to that employed in a previous 3-D GCM in which the temperature variances within a layer were explicitly determined (Hansen, et al. 1978). In the 2-D model, however, the temperature variances within a layer had to be parameterized. This parameterization is referred to as C1.

RUN	CONVECTION	ZONAL EDDIES	MOMENTUM MIXING	SYM. SST DISTRIB.
NC1-S1	MOIST (C1)	NO	NO	YES
NC1-S2	MOIST (C1)	NO	NO	YES
MC2-A	MOIST (C2)	YES	YES	NO
MD-A	DRY	YES	YES	NO
MC1-A	MOIST (C1)	YES	YES	NO
NC1-A	MOIST (C1)	YES	NO	NO

Table 3.1 The differences among the runs with respect to moist convection parameterizations, large-scale zonal eddy forcing, vertical momentum mixing, and meridionally symmetric sea surface temperature distributions are shown.

The six different experiments analyzed in this section are referred to as MC2-A, MD-A, MC1-A, NC1-A, NC1-S1, and NC1-S2. Runs MC2-A, MD-A, and MC1-A all contained explicitly specified (from a 3-D control run) large-scale zonal eddy forcing as well as vertical momentum mixing, while runs NC1-S1 and NC1-S2 had neither of these and run NC1-A had only large-scale zonal eddy forcing. Run MC2-A utilized the C2 parameterization, run MD-A had no moist convection, and runs MC1-A, NC1-A, NC1-S1, and NC1-S2 all used the C1 parameterization as well as the constraint of constant *relative* humidity within a grid box instead of constant *specific* humidity. Runs MC2-A, MD-A, MC1-A, and NC1-A all had meridionally asymmetric SST distributions corresponding to January conditions, and runs NC1-S1 and NC1-S2 had meridionally symmetric SST distributions with the meridional SST gradient in run NC1-S2 being twice that in run NC1-S1. The properties of the runs are summarized in Table 3.1. The horizontal resolution in the model was 7.8^{o}, with nine sigma levels in the vertical. The nine levels included 959 mb, 894 mb, 786 mb, 633 mb, 468 mb, 321 mb, 201 mb, 103 mb, and 26 mb. Temperature, geopotential height, and specific humidity values were available at latitudes (4 + 7.8J)N, where N = -1, +1, and J = 0,1,....11 at each of the nine levels. Values for the streamfunction and vertical velocity were also available at these latitudes, but at the eight intermediate levels. The zonal and meridional wind components were available at latitudes (0 + 7.8J)N, where N = -1, +1, and J = 0,1,....11 at each of the nine levels.

3.2 Computation of M and S^* Fields

The model output temperature data used in the analyses were only available to the nearest degree centigrade. Hence, calculation of meridional temperature gradients with these numbers, particularly near the equator, would have proven to be quite noisy. This problem was somewhat resolved by fitting a second degree polynomial to the temperatures at each level so that the resulting temperature data at each grid point was available to the nearest tenth of a degree centigrade. These new temperature values were then used for all subsequent calculations.

One assumption of the theory is that a parcel conserves its saturated moist entropy in the rising branch of the Hadley Circulation above the top of the PBL. In this study, the top of the PBL was taken to be at the lifting condensation level (LCL), which had to be determined. This level could have been determined exactly by calculating the pressure at which a "surface" parcel lifted dry-adiabatically became saturated. This method however, would not have proven very beneficial since the condensation level would more than likely not have coincided with one of the model levels. Hence, values for the other field variables would have had to be obtained through interpolation. Moreover, it was determined that, for the region of interest (35S to 35N), the LCL was either at the lowest or next higher level of the model.

The "placement" of the LCL really only affected the profile for saturated moist static entropy, S^*, since below this level, it was assumed that a parcel conserves its moist static entropy, S. Thus, the S^* profiles were obtained by calculating, at each gridpoint, the

value of S^* according to

$$S^* = \begin{cases} C_p \ln(T) - R \ln(P) + \dfrac{L_v w^*}{T} & \text{above the LCL} \\ C_p \ln(T) - R \ln(P) + \dfrac{L_v w}{T_C} & \text{below the LCL} \end{cases} \qquad (19)$$

where T = temperature in Kelvin ,

T_C= condensation temperature

C_p= 1004 J/kgK ,

R = 287 J/kgK ,

P = pressure in Pa ,

L_v= 2.5×10^6 J/kg ,

w^*= saturated specific humidity ,

w = specific humidity.

Values for w were available from the data set, while values for w^* were calculated according to :

$$w^* = \frac{\varepsilon e_0}{P} \exp\left\{ \frac{L_v}{R_v} \left(\frac{1}{T_o} - \frac{1}{T} \right) \right\} \qquad (20)$$

where ε = 0.622 ,

e_0 = 611 Pa ,

R_v = 461 J/kgK ,

T_0 = 273 K .

Values for S^* could have equivalently been calculated from the expression :

$$S^* = C_P \ln(\Theta_e^*) \tag{21}$$

where $\Theta_e{}^*$ is the saturated equivalent potential temperature. The only difference between the two expressions is a constant value of $R \ln(P_0)$, which would not have affected the calculation of derivatives of S^*.

The M profiles and absolute angular momentum profiles were obtained using calculated values of each quantity at those data points where zonal wind values were available. The quantities were calculated according to the expressions :

$$M = u - \frac{1}{2}\beta y^2 \tag{2}$$

$$AM = (u + \Omega a \cos\phi) a \cos\phi \tag{22}$$

where u = zonal wind at y,

β = 2.28×10^{-11} $s^{-1}m^{-1}$,

Ω = $2\pi/(24 \times 3600)$ s^{-1},

a = 6.4×10^6 m ,

y = distance from equator in m ,

ϕ = latitude .

3.3 Analysis of M, AM, S^*, and Φ Fields

The first major assumption of the theory which was investigated was that implied by Eq. (10), i.e. that S^* and M are conserved by ascending parcels above the PBL. This was investigated first by examining profiles of S^* and M as well as profiles of the streamfunction and absolute angular momentum for each of the runs. The results are shown in Figures 3.1 - 3.4. Figure 3.1 shows profiles of absolute angular momentum superimposed on streamlines. Examination of this figure is helpful to identify areas where absolute angular momentum is being conserved by ascending parcels. The solid and dashed lines are for the streamfunction, with dashed lines denoting negative values. The dotted lines are lines of constant absolute angular momentum. The horizontal axis is latitude and the vertical axis is pressure in millibars.

Figure 3.1a (run NC1-S1) shows an almost constant valued streamfunction. Hence, the meridional circulations are quite weak and not very well defined. A single, weak ITCZ is centered near 4N. The absolute angular momentum lines flare outward quite a bit with two maxima centered near 10N and 10S above 201 mb. This pattern is consistent with the absence of vertical momentum mixing for this run.

Figure 3.1b (run NC1-S2) shows a very complicated looking streamfunction with a region of very intense rising motion near 12S at low levels and tilted equatorward in the vertical. The latitudinal extent of the descent regions on either side is quite large, extending from 12S in the southern hemisphere and 4N in

the northern hemisphere. The meridionally asymmetric pattern is prominent despite a symmetric SST distribution. Again, as in run NC1-S1, the absolute angular momentum lines flare outward, being even more pronounced for this run, particularly at upper levels at subtropical latitudes. The inward flaring at low levels is indicative of the strong easterlies present at tropical latitudes.

Figure 3.1c (run MC2-A) shows two separate, relatively intense meridional cells, with the northern hemisphere one being the more intense of the two. Vertical motions are weak and somewhat unresolvable (from the figure) in the region from 12S to 4N. Rising motion extends on either side of this band to 23S and 20N. Absolute angular momentum lines flare only slightly outward for this run at mid and upper tropospheric levels. Unlike that indicated in runs NC1-S1 and NC1-S2, however, maximum "flaring" occurs at subtropical latitudes (~23N and ~23S) rather than at more tropical latitudes (~15N and ~15S) in the upper troposphere.

Figure 3.1d (run MD-A) shows some similarities in both fields to those in figure 3.1b. Recall that this run contained no moist convection. Again a single ITCZ is present and is quite intense. Centered near 4N at low levels, it zigzags its way into the southern hemisphere at upper levels. The ascent region is quite evident, extending from 12S to 12N. There is a slight equatorward tilt with height of the northern boundary, but none for the southern one. The structure of the absolute angular momentum field is also similar to that of run NC1-S2. The shape of these lines, particularly at lower latitudes, is consistent with the intense meridional circulations which are the result of the absence of moist

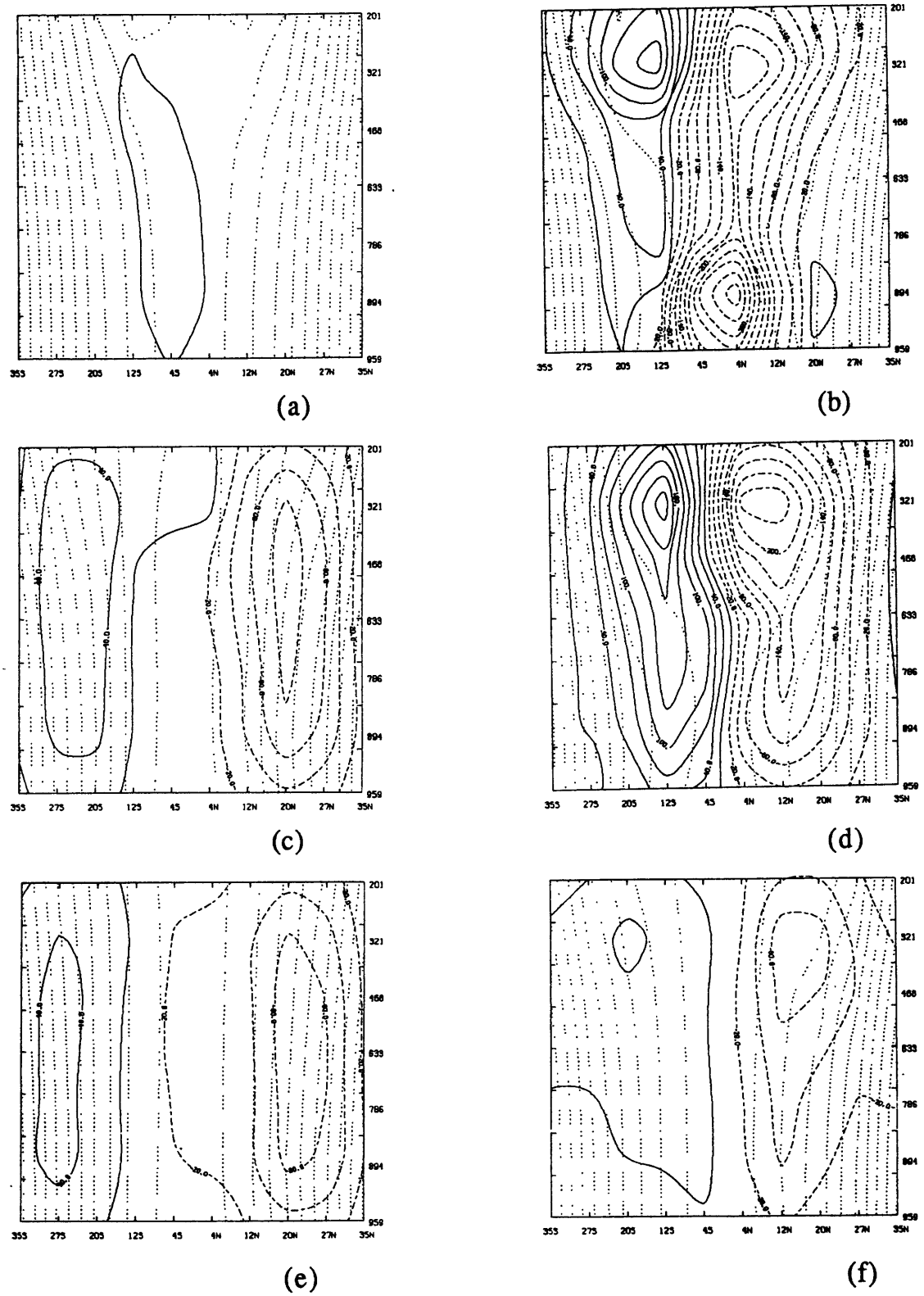

Figure 3.1 Latitude-pressure contour plots of streamfunction (solid (>0) and dashed (<0) lines, interval is 10^9 kg/s) and absolute angular momentum (dotted lines, interval is 10 m^2/s) for the six 2-D model runs: (a) NC1-S1, (b) NC1-S2, (c) MC2-A, (d) MD-A, (e) MC1-A, and (f) NC1-A.

convection. The absence of moist convection leads to a decrease in static stability, causing accelerated meridional circulations. It is important to note that, although the profiles for runs NC1-S2 and MD-A appear similar, a major distinction between the two is the presence of momentum mixing in run MD-A and the absence of it in NC1-S2.

Figure 3.1e (run MC1-A), likewise, is similar to figure 3.1c. This is not surprising, however, since the moist convective parameterizations for runs MC2-A and MC1-A differed only slightly from each other. In this figure, the two ITCZ's are slightly weaker than their counterparts in Figure 3.1c, with the southern hemisphere cell being displaced slightly farther south as well. The vertical motions are again very weak and undefinable between 4S and 12N. The absolute angular momentum lines, despite being almost vertical, especially near the equator, actually do follow the streamlines in the ascent regions except near the levels of the return flow of the two cells.

Figure 3.1f (run NC1-A) shows a double ITCZ once again, with the one in the northern hemisphere being much stronger than the one in the southern hemisphere. Although harder to discern (from the figure) in the southern hemisphere, the region of rising motion extends to 12N, with a slightly poleward tilt with height of this boundary. The absolute angular momentum lines in the northern hemisphere are quite flared at upper levels in subtropical latitudes but at lower latitudes do not seem to be as parallel to the streamlines as they are to those in the southern hemisphere.

In summary of figure 3.1, the amount of "flaring" of the

absolute angular momentum lines for a particular run, seems dependent on either the absence of vertical momentum mixing or the presence of intense meridional circulations. Too intense of a meridional circulation though, results in a complicated cell structure so that absolute angular momentum no longer appears to be conserved by ascending parcels. The runs in which ascending parcels do appear to conserve absolute angular momentum are NC1-S1, MC2-A, MC1-A, and NC1-A.

In figure 3.2, the profiles of S^* and M are plotted for each of the six runs. Examination of this figure is necessary to identify areas where the M and the S^* fields are congruent. The word congruent here means that Eq. (10) is valid. The congruency of the two fields can be visibly assessed from the parallel nature between the two sets of contour lines. The solid lines are lines of constant S^* while the dotted and dashed lines are lines of constant M. The dotted lines are spaced every 10 m/s apart while the dashed lines are spaced every 4 m/s apart. The actual values are not necessary since it is only the shape of the lines which need be visible. Although the field is not labeled, it will suffice to say that it has a maximum near the equator and decreases outward on both sides. As an overall observation of figure 3.2, it can be seen by comparison with figure 3.1, that the profiles of M qualitatively resemble those of the absolute angular momentum (i.e. although the actual values and gradients differ, the shapes of the two sets of lines are similar).

In figure 3.2a (run NC1-S1), S^* increases with height throughout the region. The meridional symmetry of both fields

coincides well with the symmetric SST distribution for this run. In the ascent region from the equator to 8N, some congruence between the two fields is evident.

In figure 3.2b (run NC1-S2) the contoured entropy field reflects the very intense gradients of the symmetric SST distribution. Very high values are present all the way down to 959 mb near the equator, while the somewhat lower values at this level found between 4N and 20N are due to the intense equatorward advection of cooler air from more poleward latitudes. Although there is some congruence between the two fields in the ascent region (12S to 4N) at mid levels, particularly from 12S to 4S, it diminishes greatly above 400 mb. This is evident, despite the absence of momentum mixing in this run.

In figure 3.2c (run MC2-A) the maximum entropy values overlie the maximum SST, near 4S. The slight "bowing in" of the entropy lines from 959 mb up to 786 mb is due to the equatorward flow in this region, bringing in slightly cooler air. This "bowing in" is more prominent in the northern hemisphere because of the stronger meridional circulation there. Despite the momentum mixing which was present in this run, there is some congruence between the two fields in the ascent region, away from the equator, i.e. 20S to 14S and 14N to 20N. This diminishes greatly, however, at upper levels. This perhaps is an indication of more vigorous mixing at the tropopause than at lower levels, although this will be investigated more quantitatively later in this section.

In figure 3.2d (run MD-A) the shape of the isentropes can be explained by the strong equatorward motions at low levels,

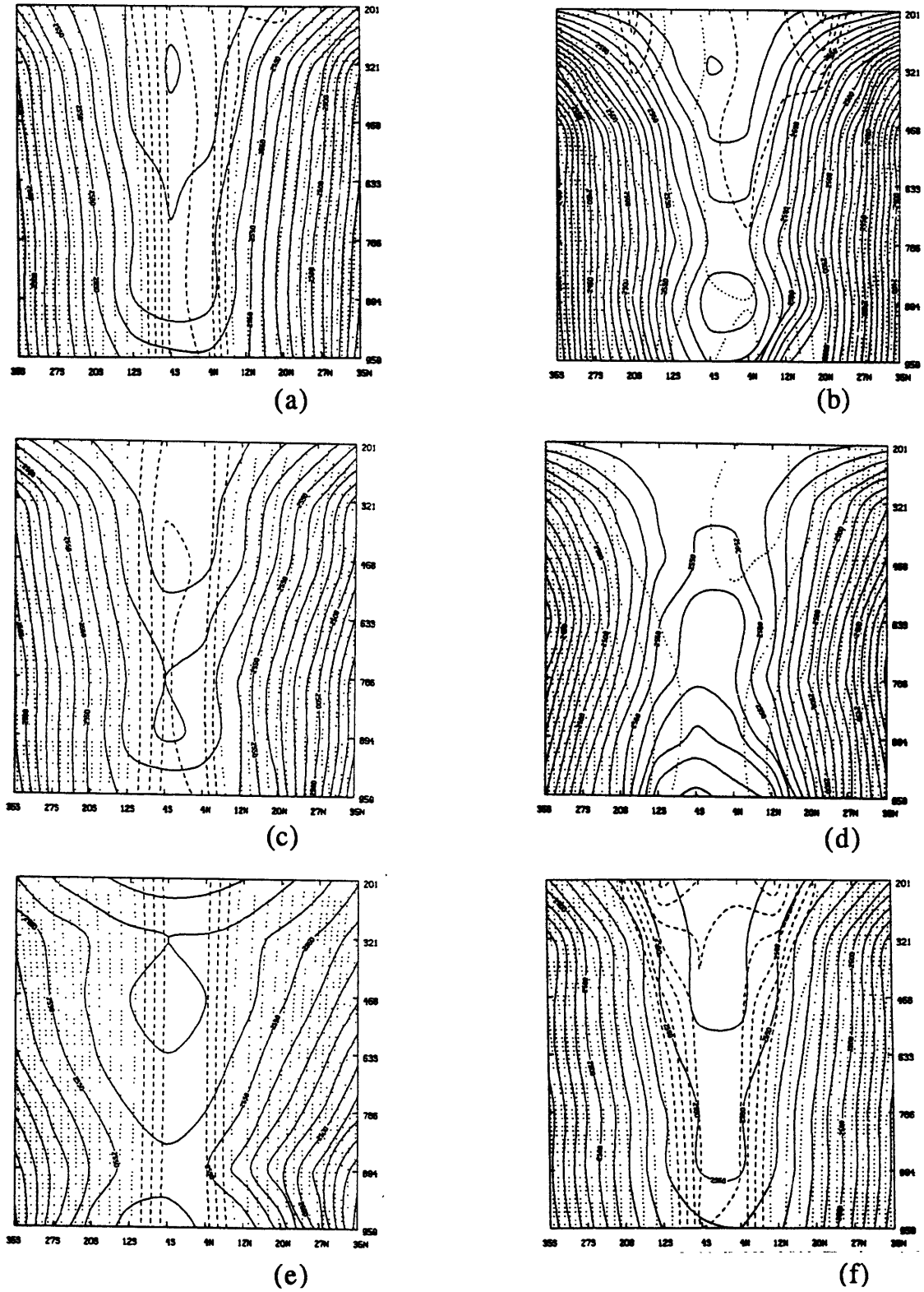

Figure 3.2 Latitude-pressure contour plots of saturated moist entropy (solid lines, interval is 10 J/kgK) with LCL = 959 mb and M (dotted (interval is 10 m/s) and dashed (interval is 4 m/s) lines) for the six 2-D model runs: (a) NC1-S1, (b) NC1-S2, (c) MC2-A, (d) MD-A, (e) MC1-A, and (f) NC1-A.

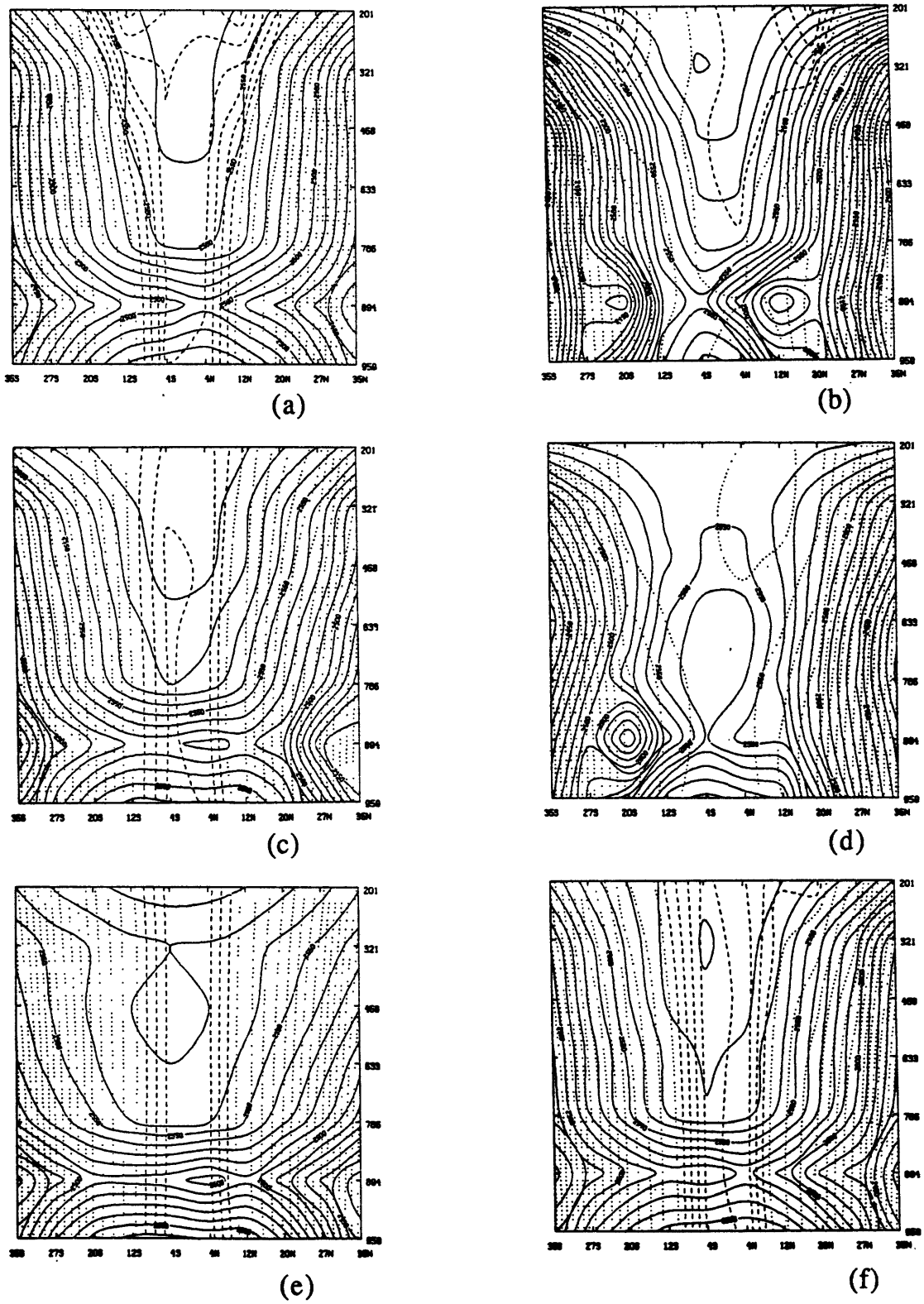

Figure 3.3 Identical to figure 3.2 except for LCL = 894 mb.

along with the strong ascent near the equator. The "bowing in" is more pronounced in this run than in the previous one, and extends to much higher levels in the southern hemisphere. It is likely that radiational cooling is sufficiently large in the rising branch so that the S^* profile exhibits relatively lower values in ascent regions. The M profile is similar to that in figure 3.2b, but more importantly, it is obvious that nowhere in the ascent region is there any congruence between the two fields.

Comparing figure 3.2e (run MC1-A) with figure 3.2c reveals lower values of S^* at low levels (where the lines appear "bent") and slightly higher values at mid levels in subtropical latitudes. This is explained by realizing that the different moist convection scheme utilized in run MC1-A resulted in enhanced convection at these latitudes. This would account for the higher values at upper levels, while the resulting increase in precipitation and subsequent evaporative cooling at lower levels would account for the lower values below. Also the overall meridional temperature gradient is weaker than that indicated in figure 3.2c, which is consistent with the reduced intensity of the meridional circulations. The M field, on the other hand, has almost no structure in the vertical. The congruence between the two fields for this run is virtually non-existent.

In figure 3.2f (run NC1-A) similarities in the S^* field to that in figure 3.2c can be seen. The absence of momentum mixing from this run, however, has resulted in visibly more congruence between the two fields in the ascent region (12S to 12N).

Figure 3.3 is identical in format to figure 3.2 but illustrates

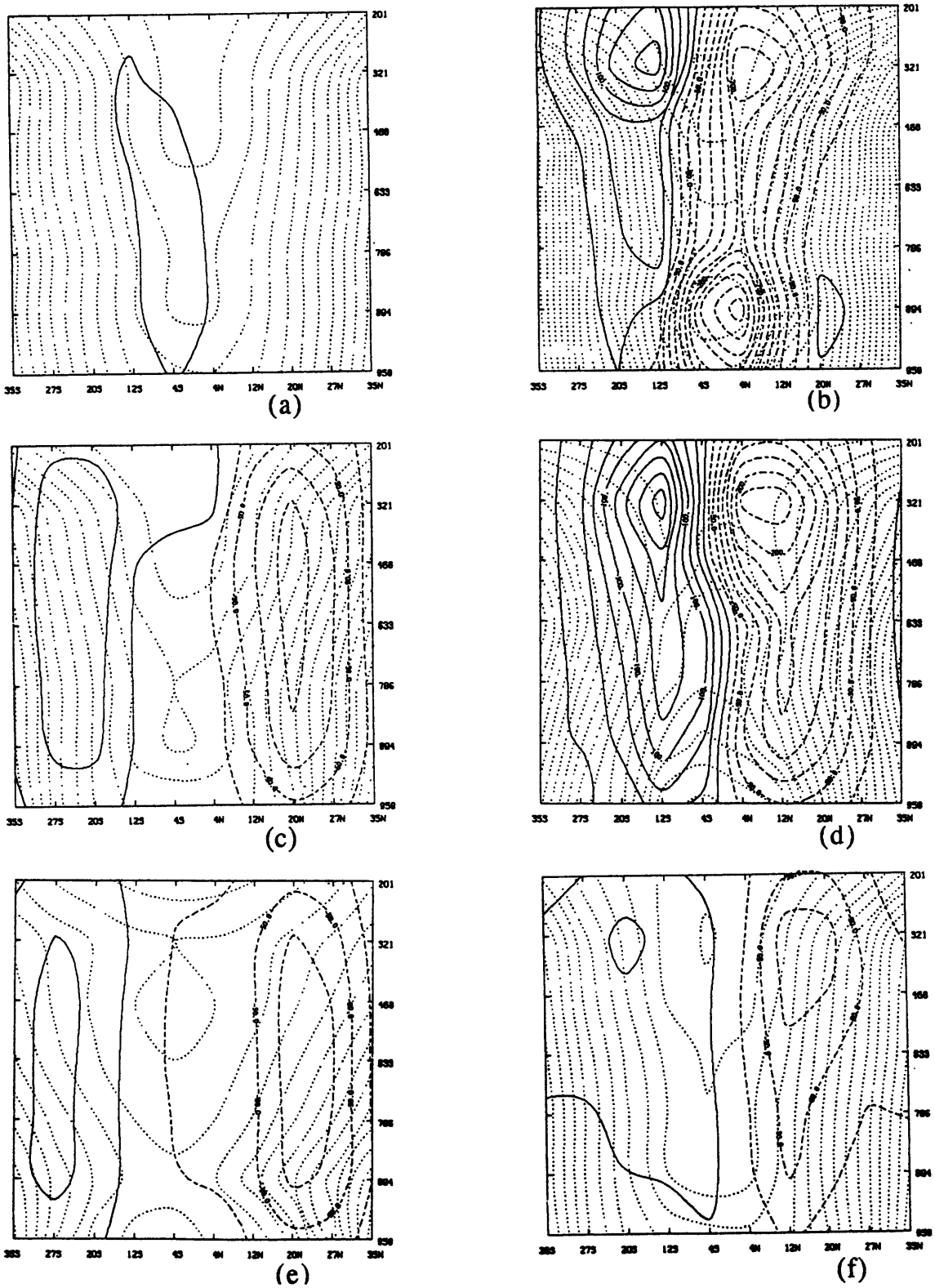

Figure 3.4 Latitude-pressure contour plots of streamfunction (solid (>0) and dashed (<0) lines, interval is 10^9 kg/s) and saturated moist entropy (dotted lines, interval is 10 J/kgK) for the six 2-D model runs: (a) NC1-S1, (b) NC1-S2, (c) MC2-A, (d) MD-A, (e) MC1-A, and (f) NC1-A.

the saturated moist entropy profiles based on the assumption that the top of the PBL is at 894 mb. The contouring of the saturated moist entropy field is markedly different below 894 mb in all of the runs except for NC1-S2 and MD-A. This is perhaps an indication that the LCL for these two runs was closer to 894 mb than to 959 mb. The higher LCL can be accounted for by realizing that these two runs had the most intense meridional circulations associated with them and thus drier boundary layers than in the other four runs.

Figure 3.4 shows the streamfunctions from figure 3.1 superimposed on the S^* fields from figure 3.2 for each of the runs. Whereas Figure 3.1 indicates those runs in which ascending parcels conserved absolute angular momentum, and Figure 3.2 indicates those runs for which the S^* and M fields were congruent, Figure 3.4 indicates those runs in which ascending parcels conserved S^*. For those runs indicating incongruity, examination of this figure in conjunction with Figure 3.1 is necessary to determine which of the two quantities is not being conserved. To varying degrees, results indicate that S^* is not a conserved quantity of ascending parcels in any of the runs. Results from runs NC1-S1 and NC1-A indicate this to a lesser extent while results from the other four runs give a clearer indication of this. The degree of non-conservation seems proportional to the intensity of the ascent.

In summary of figures 3.2 - 3.4, it can be said that only in runs NC1-S1 and NC1-A is there a sense of congruence between the S^* and M fields in the ascent regions due to both being partially conserved quantities. Run MC2-A shows the same to a lesser

extent, while for the other three runs congruence between the two fields is visibly poor. The incongruity is the result of $S^*$and M being independently not conserved quantities in varying degrees.

The validity of Eq. (10) is now examined more quantitatively. Equation (10) states that, following a constant S^* line, the M field must remain constant as should the value for the derivative, dM/dS^*, taken in any direction. This was examined by first calculating dM/dS^* in the y-direction (along constant pressure) at a low level near the top of the PBL. These values were then compared to those obtained by calculating dM/dS^* in the P-direction (along constant latitude) for the region above the PBL. Additionally, values of dM/dS^* in the y-direction were calculated at levels above the top of the PBL to determine the validity of the assumption at upper levels.

Figure 3.5 shows the calculated values of dM/dS^* in the y-direction along with the saturated moist entropy profile at 934 mb (near the top of the PBL) for each of the six runs. The graphs show the derivative to be nearly a constant between 1 and 2 K/(m/s), with latitude. The "spikes" correspond to the flat regions of the S^* profiles. The constant-valuedness of the dM/dS^* profile was further investigated to determine if a significant correlation existed between the saturated moist entropy and the M fields. Results, however, revealed only that the quadratic nature of the M field (completely dominated by the $(1/2)ßy^2$ term) was spuriously correlated with the quadratic nature of the S^* field, especially at higher latitudes. The quadratic behavior of the S^* field was, in turn, a reflection of the quadratic-like SST distribution below.

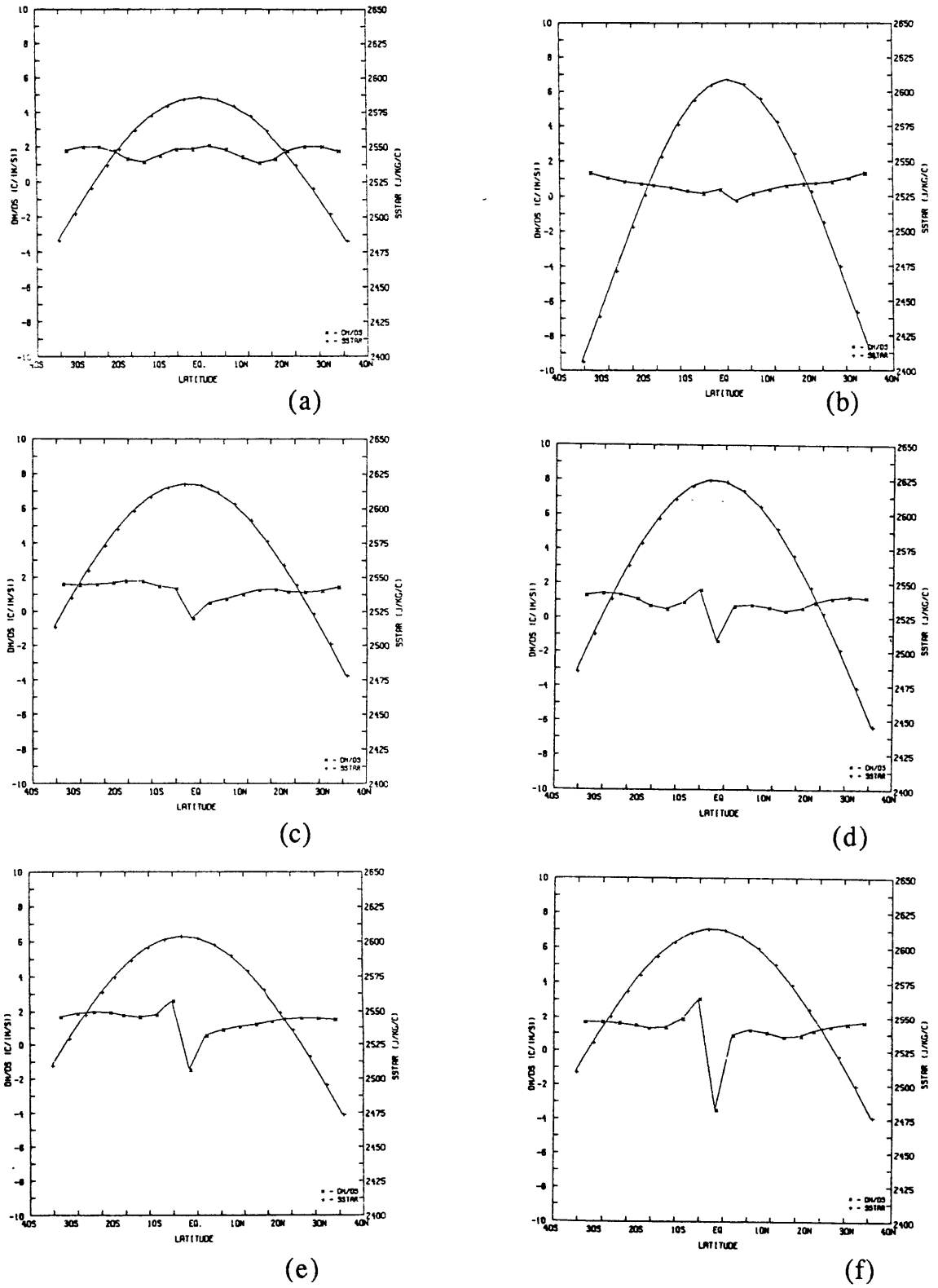

Figure 3.5 Profiles of dM/dS* (+) calculated in the y-direction and S* (*) at 934 mb for the six 2-D model runs: (a) NC1-S1, (b) NC1-S2, (c) MC2-A, (d) MD-A, (e) MC1-A, and (f) NC1-A.

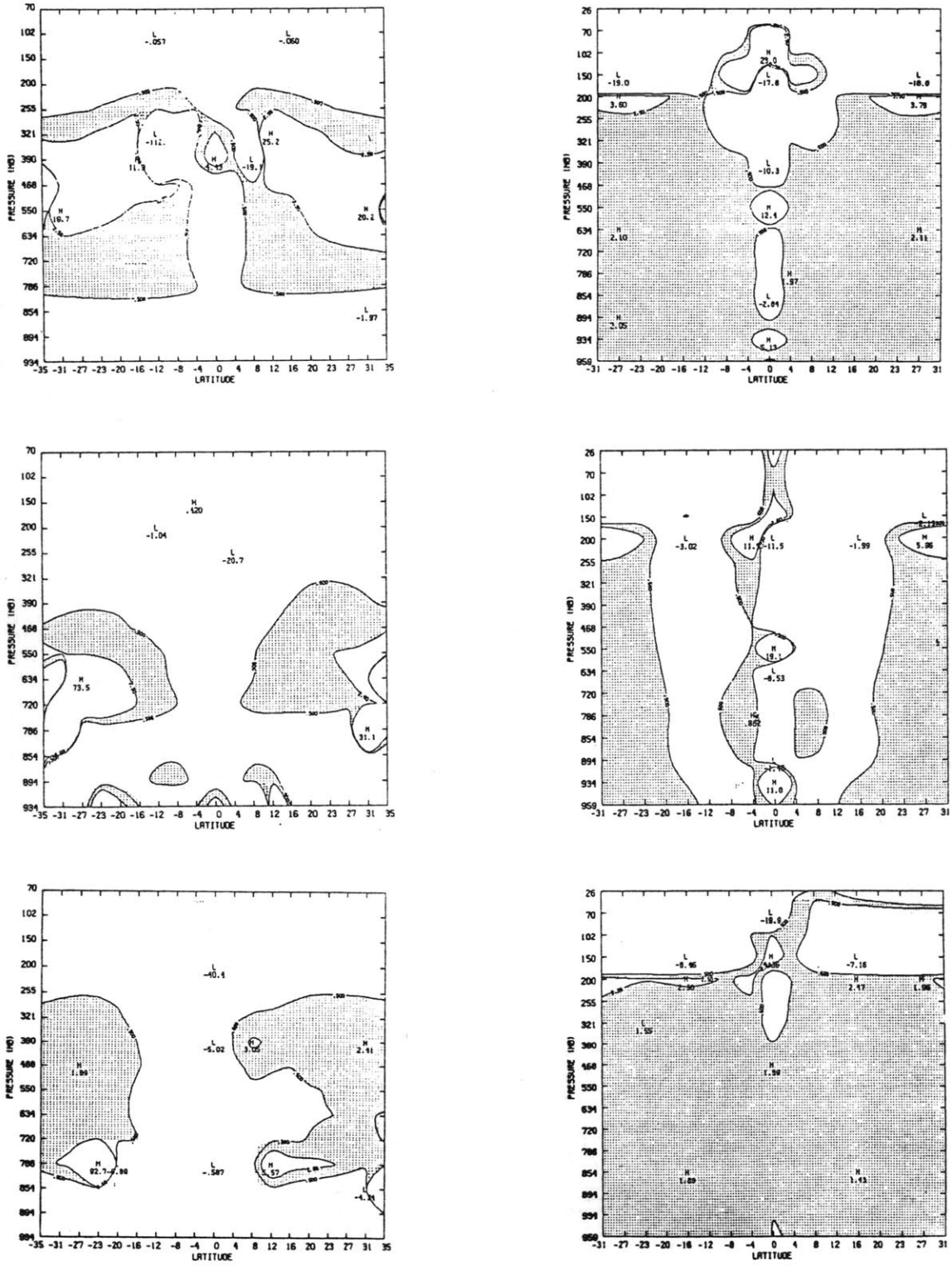

Column A Column B

Figure 3.6 Latitude-pressure contour plots of dM/dS^* calculated in the P-direction (column A) and in the y-direction (column B) for runs NC1-S1 (top), NC1-S2 (middle), and MC2-A (bottom). Shading indicates values between 1.0 and 2.0 °C/(m/s)

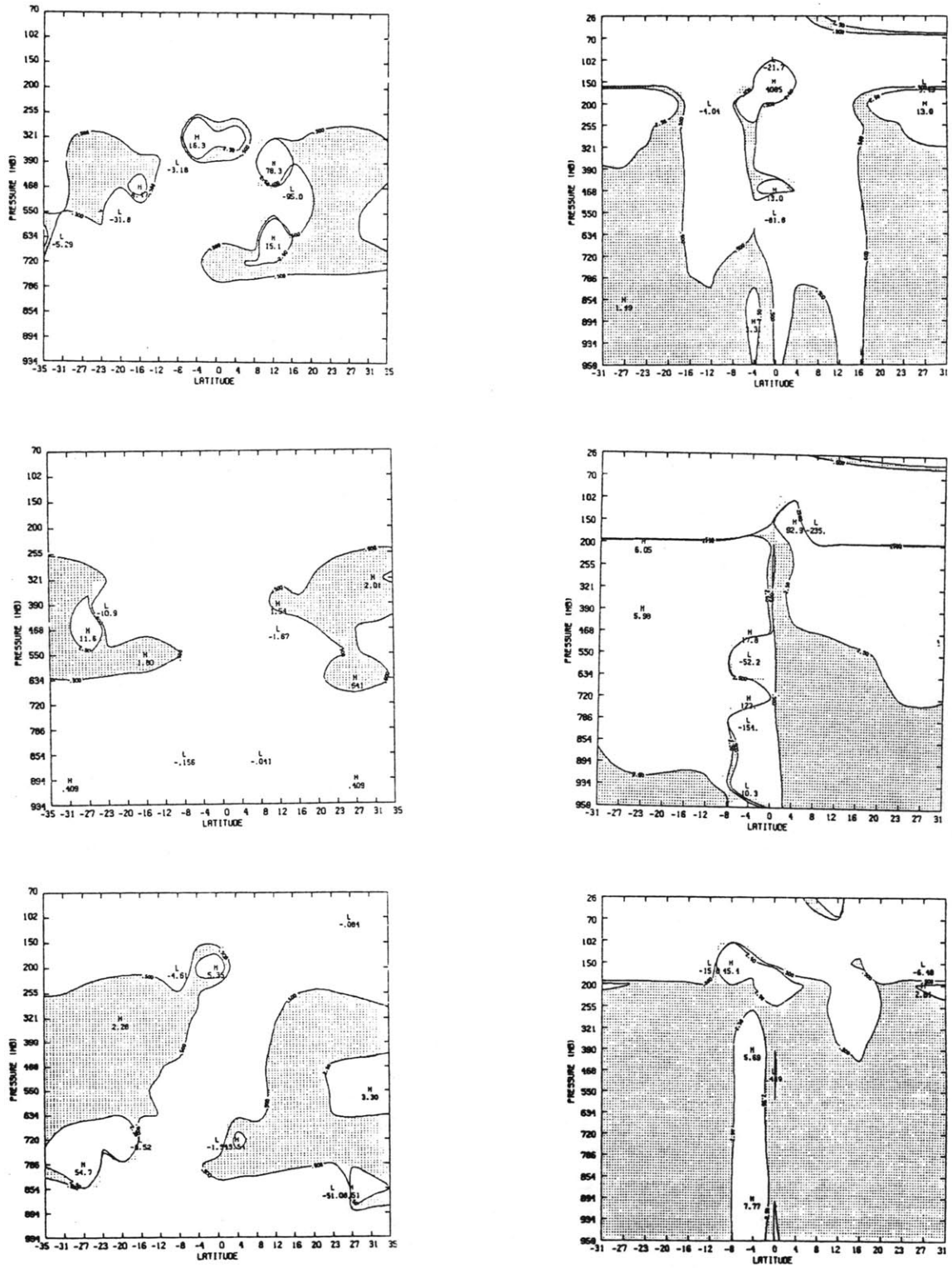

Column A Column B

Figure 3.6 (cont'd) Runs MD-A (top), MC1-A (middle), and NC1-A.

Figure 3.6 shows a comparison between dM/dS^* calculated in the y-direction and dM/dS^* calculated in the P-direction. The graphs in column A correspond to the P-direction and the graphs in column B correspond to the y-direction. Regions between 1.0 and 2.0 K/(m/s), which is a mean range of the values at 934 mb, are shaded. Ideally, if perfect congruence between the two fields existed, the contour lines of the plots would follow the contour lines of both the S^* and M fields. Inspection of the graphs reveals that, while this is not the case, some verification of Eq. (10) is indicated by runs NC1-S1, MC2-A, and NC1-A. This conclusion can be arrived at after observing the amount of overlap in the ascent regions between the "A" and "B" graphs for each run.

3.4 Ekman Velocity Assumption

The second major assumption of the theory which was investigated was that the vertical velocity at the top of the PBL was frictionally driven and could be determined by Ekman pumping theory. Figure 3.7 shows plots for each run of the calculated Ekman velocity as it compares to the actual vertical velocity at the second lowest model level. The Ekman velocity was calculated according to Eq. (16) :

$$w_E = -\left(\frac{du}{dy}\right)\frac{|f|}{f}\sqrt{\frac{K}{2|f|}} \qquad (16)$$

Values for K were obtained using the parameterization (Hansen, et al., (1983)) :

$$K = \begin{cases} \dfrac{\left(60 - 1.156\text{x}10^{7}\dfrac{d\Theta}{dz}\right)}{\left(1 - 1.752\text{x}10^{4}\dfrac{d\Theta}{dz}\right)} & , \quad \dfrac{d\Theta}{dz} < 0 \\ \dfrac{60}{(1 + 50\text{Ri}_{PBT})} & , \quad \dfrac{d\Theta}{dz} > 0 \end{cases}$$

where Ri is the Richardson number given by :

$$\text{Ri}_{PBT} = g\frac{\Delta\Theta\Delta Z}{T_{PBT}(\Delta u^2 + \Delta v^2)}.$$

The parameters T, Θ, z, u, and v have their usual meanings and Δ's refer to the change in a quantity from the surface to the top of the boundary layer (PBT). Values for K were calculated using surface and 894 mb level data. Values of Δu and Δv were calculated assuming no wind at the surface. The values for du/dy in Eq. (16) were obtained from zonal velocity data from the model runs.

Inspection of figure 3.7 shows the calculated Ekman and model vertical velocities to be of comparable magnitudes. Four of the six model runs have vertical velocity magnitudes, as will be shown later, comparable to those found at low levels in the Earth's atmosphere. It is important to realize that because zonal wind and vertical velocity model data were available on staggered levels, the calculated Ekman and model vertical velocity profiles do not

correspond to the same level. The model velocities are for a pressure level of 854 mb and the calculated velocities are for a pressure level of 894 mb. In three of the four runs with realistic vertical velocity magnitudes, the model indicates peak magnitudes greater than those of the calculated Ekman profile. This may be due in part to the model level being slightly above the actual top of the PBL. The larger magnitudes exhibited by the model at this level seem consistent with the fact that it is almost always the case that vertical velocity magnitudes are greater above the top of the PBL rather than right at it.

Figure 3.7a (run NC1-S1) does not show very good correlation between the calculated Ekman and model vertical velocity profiles. While the model data indicates a sharp, single ITCZ near 4N, the Ekman profile indicates a broader, weaker ITCZ centered near the equator with two, weaker ascent regions on either side located at 20S and 20N. The meridional symmetry of the Ekman profile reflects the meridional symmetry of the zonal wind profile at that level. Recall that run NC1-S1 had a meridionally symmetric, sinusoidal SST profile, though this does not seem to be reflected by the model vertical velocity profile.

Figure 3.7b (run NC1-S2) again does not show a very good correlation between the calculated Ekman and model vertical velocity profiles. The model data indicates a very intense region of ascent centered near 4S with a very intense region of descent centered near 4N. The Ekman profile is again quite meridionally symmetric with a very broad, intense region of descent extending to 20 degrees on either side of the equator. Again, this meridional

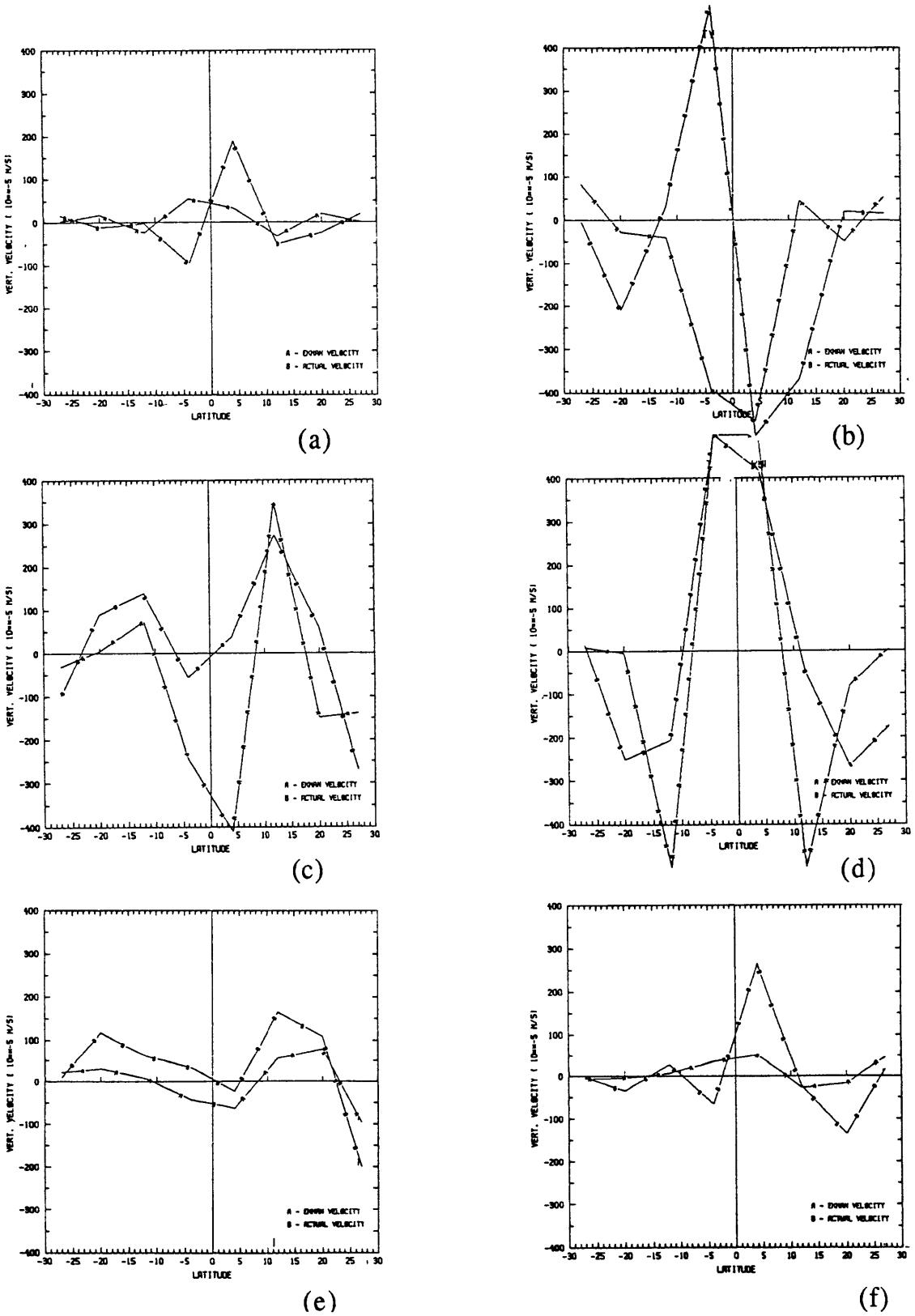

Figure 3.7 Ekman vertical velocities (A) calculated at 894 mb and model vertical velocities (B) at 854 mb for the six 2-D model runs: (a) NC1-S1, (b) NC1-S2, (c) MC2-A, (d) MD-A, (e) MC1-A, and (f) NC1-A.

symmetry seems a reflection of the meridionally symmetric SST distribution. The model vertical velocity profile does not show this.

Figure 3.7c (run MC2-A) shows a good amount of correlation between the calculated Ekman and model vertical velocity profiles. The two peaks of ascending motion in each profile coincide exactly and are of comparable magnitudes, with the one at 12N being stronger than the one at 12S. The descent region indicated by the model data is, however, much smaller and weaker than that indicated by the calculated Ekman profile.

Figure 3.7d (run MD-A) shows good correlation between the calculated Ekman and model vertical velocity profiles despite the magnitudes of both being unrealistically large. Both profiles indicate good meridional symmetry with a single, very intense ITCZ extending 10 degrees on either side of the equator. The descent regions on either side are much more intense for the calculated Ekman profile.

Figure 3.7e (run MC1-A) also shows good correlation between the calculated Ekman and model vertical velocity profiles. The two ascent regions are weaker and broader than those in run MC2-A. Also the descent region indicated by the calculated Ekman profile is much broader and stronger than that indicated by the model vertical velocity profile.

Figure 3.7f (run NC1-A) shows poor correlation between the calculated Ekman and model vertical velocity profiles. The model profile shows a well defined ascent region centered at 4N, a smaller, weaker ascent region at 12N, and a descent region located between the two. The calculated Ekman profile shows a very weak

and broader region of ascent extending from 12S to 10N.

In summary, there is good correlation between calculated Ekman and model vertical velocity profiles in three of the six runs : MC2-A, MD-A, and MC1-A. Good correlation and meridional symmetry exist for run MD-A despite unrealistically large vertical velocity magnitudes and an asymmetric SST distribution. The other three runs: NC1-S1, NC1-S2, and NC1-A show poor correlation between calculated and model vertical velocity profiles, particularly near the equator. The calculated vertical velocity profiles for runs NC1-S1 and NC1-S2 do, however, exhibit good meridional symmetry as do the SST distributions in these cases, while the model vertical velocity profiles do not. The poor correlations in the two runs with symmetric SST distributions is somewhat puzzling but may be an indication that the steady state model vertical velocity profiles for these runs were somewhat noisy. This idea is supported by the fact that the vorticity patterns at 854 mb are similar (and meridionally symmetric) to each other while the vertical velocity profiles at 854 mb are neither similar nor meridionally symmetric to each other.

More quantitative correlations are difficult to assess due to the specification of K, the eddy viscosity coefficient in Eq. (16), which is a difficult quantity to parameterize properly. For purposes described here, the abovementioned method is no less inadequate than others. With this parameterization, though, difficulty in accurately determining K did stem from an inaccurate determination of the stability of the surface layer, i.e. in determining $d\Theta/dz$. Since the sign of the calculated velocities was

not a function of this, however, the location of the ascent and descent regions was not affected, although the location of the peaks within the regions may have been.

3.5 Meridional Temperature Gradients

The third assumption which was investigated was that the meridional temperature gradient at the top of the PBL was equal to that at the surface. Values of the meridional temperature gradient, dT/dy, were calculated at the top of the PBL and at the surface. Gradient values were obtained at intermediate latitudes where temperature data was available, using values at successive data points. Figure 3.8 summarizes the results. For each run, dT/dy was calculated at the two lowest sigma-levels using the smoothed temperature data. Meridional SST gradients were also calculated in a similar manner, although the actual temperatures from the model runs were used since they were available to the nearest 0.1°C.

As can be seen from the plots, the meridional temperature gradients at the two lowest levels are very close to those at the ocean surface. The agreement is slightly better in those runs where the SST is specified as a sine function, although this may just be an artifact of the smoothing method used. In all cases, however, the assumption that the temperature gradient at the top of the PBL is equal to that at the surface seems a valid one. This is no surprise, since from mixing-layer theory, it is known that potential temperature and specific humidity are conserved quantities in this layer.

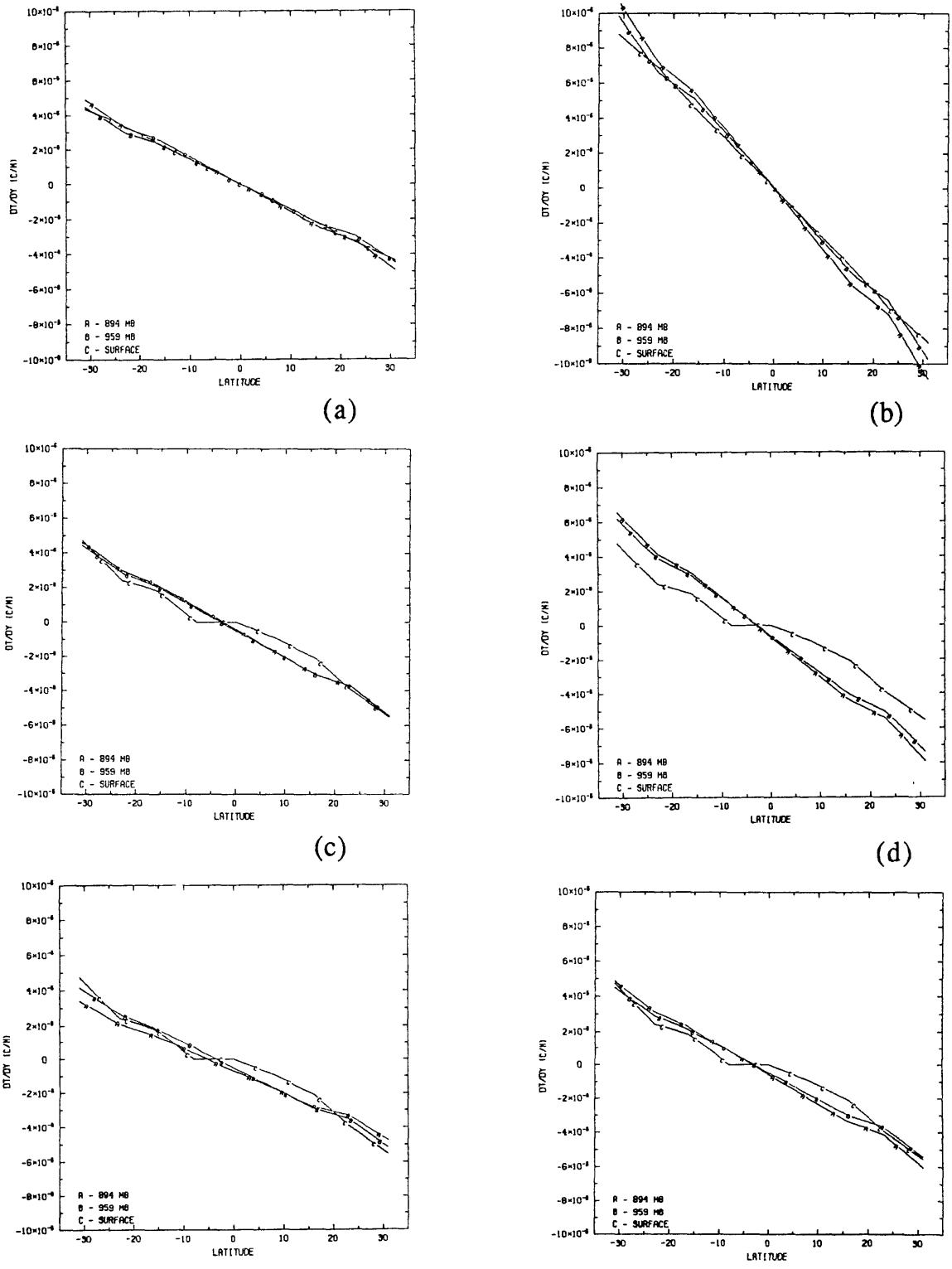

Figure 3.8 Meridional temperature gradients at 894 mb (A), 959 mb (B), and at the surface (C) for the six 2-D model runs: (a) NC1-S1, (b) NC1-S2, (c) MC2-A, (d) MD-A, (e) MC1-A, and (f) NC1-A.

3.6 Theoretical Vorticity

The first prediction of the theory which was investigated was that stated in Eq. (15) :

$$\frac{du}{dy} = \beta y + 2\left(\frac{\partial S^*}{\partial y}\right)\left(\frac{T(y) - T(y_o)}{\beta(y_o^2 - y^2)}\right) \quad . \qquad (15)$$

The quantity y_0 is taken as the latitude at which the large-scale vertical velocity changes from upward to downward. Actually it is not so important, as far as the calculations are concerned, that y_0 be taken as this latitude so much as it is that it be taken somewhere within the ascent region and poleward of the latitude in question. This can be done, since the theory does not "feel" the other side of y_0 in terms of the dynamics and thermodynamics (a more formal approach to determining y_0 would consist of matching boundary conditions across y_0 with a solution for the descending branch of the Hadley Circulation). Intuitively, this can be seen to be valid since the value for du/dy at a particular latitude should not change depending upon where in the ascent region y_0 is selected. This non-constraint was taken advantage of in the calculations for two reasons. One reason was to avoid the difficulty of accurately determining y_0 due to the coarse resolution of the vertical velocity data. The other reason was to investigate the behavior of the calculated value of du/dy as a function of y_0. Theoretically, the calculated value of du/dy at a particular latitude should be

independent of y_0 provided that it is within the ascent region and poleward of the latitude in question and also provided that $T(y_0)$ is correctly specified.

Since the ascent region for most of the runs extended only to approximately 20^o on either side of the equator, comparison of theoretical calculations with model data would be limited to at most four latitudes (12S, 4S, 4N, and 12N) for each run. Therefore, in order to increase the number of latitudes which could be investigated, values of pertinent quantities (i.e. temperature and zonal wind) were obtained at intermediate latitudes using a cubic-spline interpolation scheme. This resulted in available data every 3.9^o latitude. Furthermore, as an aid for determining outflow temperatures, $T(y_0)$, the data was interpolated in the vertical, again using a cubic-spline scheme, to obtain temperature data at intermediate pressure levels. The outflow temperature, $T(y_0)$, for a particular isentrope was that temperature at the level at which the isentrope crossed y_0.

Realizing that the theoretical result should hold not only at the top of the PBL but anywhere above within the ascent region as well allowed the further advantage of comparing theoretically calculated values of du/dy with those from model data at various pressure levels. The objective of this was to determine if agreement were better at some levels than at others. What ultimately was done for each run was to choose latitudes that were within ascent regions. Then values of du/dy were calculated using Eq. (15) at each chosen latitude as a function of y_0 at each of twelve levels within the troposphere. The domain of y_0 values

ranged from 35N or 35S (depending upon the hemisphere) to within one degree poleward of a chosen latitude, in increments of one degree. For example, for 12N, values for y_0 ranged from 35N to 13N. The 35 degree limit exceeded the extent of the ascent regions in all cases. The intent of this was to examine how the theoretically calculated values behaved near the ascent boundaries. The twelve levels included 959 mb, 934 mb, 894 mb, 854 mb, 786 mb, 720 mb, 633 mb, 520 mb, 468 mb, 390 mb, 320 mb, and 255 mb. It should be noted that saturated moist entropy values were used for all levels of calculation for convenience. This resulted only in slightly larger magnitudes of the dS^*/dy term in the first two or three levels and was inconsequential above this.

The results of the calculations are summarized in figures 3.9 - 3.15. In each graph, the plot is of the ratio of the theoretically calculated value of du/dy to that obtained from the model's zonal velocity data, using centered differences. The vertical axis is actually two logarithmic scales combined together, to accommodate the large variations in the ratio. The region where the graphs are split is not of interest, and so has been compressed. In each graph, an arrow points to the best guess for y_0, the latitude at which the large scale vertical velocity changes sign. The best guess was obtained through examination of the available vertical velocity data in conjunction with the streamfunction for each run.

The left column of figure 3.9 shows the results for run NC1-S1. The only latitude investigated was 4N (note that only three levels of the calculations have been shown for all the runs for conciseness). At low levels (below 700 mb), the negative signs of

both the theoretically calculated and data-calculated du/dy are consistent with Ekman pumping theory in the ascent region while at higher levels, it is difficult to ascertain the proper sign for du/dy. Also at low levels the values are quite large in magnitude and this may be attributable to having used values of saturated moist entropy within the PBL. This resulted in higher values of saturated moist entropy in the PBL, higher ouflow levels, and thus colder outflow temperatures. This caused the magnitude of the dS^*/dy term (negative in this case) to be larger than it should have been. At low and mid levels although the calculated values do not really remain constant from 5N to 10N, they are within an order of magnitude. Why the sign change occurs where it does in some of the plots is not understood, since it does not seem to correlate well with the y_0 in each case. In fact, nothing exceptional seems to occur at y_0 although at the same time it is difficult to say how the curve should behave outside of y_0, given the limitations of the present theory. At upper levels, above 500 mb, agreement is worse. Considering the proximity of the latitude to the equator, this may be a result of cross-equatorial flow (i.e. isentropes originating in the southern hemisphere at lower levels). Coarse grid size, however, limits further investigation of this. It is believed that the constraint of no momentum mixing, along with a symmetric SST distribution are the reasons for good agreement in this run.

For run NC1-S2, y_0 was chosen as 14S, and all of the latitudes investigated were in the southern hemisphere: 12S, 8S, and 4S. The last three columns in figure 3.9 show that almost all the calculated values are positive, while almost all the actual

values for du/dy are negative. Again at low levels the positive, theoretically calculated values seem consistent with Ekman pumping theory and it is puzzling why, even at the more poleward latitudes (8S and 12S), the data-calculated values are negative. Separation of the terms in Eq. (15) show the sign of the theoretically calculated values is due to the dominance of the dS^*/dy term. This is not unexpected, however, considering the magnitudes of the meridional SST gradient present in this run.

Figures 3.10 and 3.11 summarize the results for run MC2-A. In this run y_0 was determined to be 23S in the southern hemisphere and 20N in the northern hemisphere. Somewhat good agreement is evident at all three levels at latitudes 16S and 12S. Theoretically calculated values of du/dy, although not constant within the ascent region, are within an order of magnitude of the data-calculated values at these two latitudes. Worse agreement is found at 16N and 12N at all levels. Sign agreement at the other four latitudes: 8S, 4S, 4N, and 8N, is very poor, although it should be pointed out that the region between the equator and 6S is actually a region of weak descent. Despite the poor sign agreement at the other three latitudes, the theoretically calculated values of du/dy at low levels do have signs consistent with Ekman pumping theory. The good agreement at 12N and 16N, and the better agreement at 16S and 12S may be justified from the degree of congruence between the S^* and M fields at these latitudes visible in figure 3.3c. The better agreement in the southern hemisphere is present despite its weaker meridional circulation and less flared M lines.

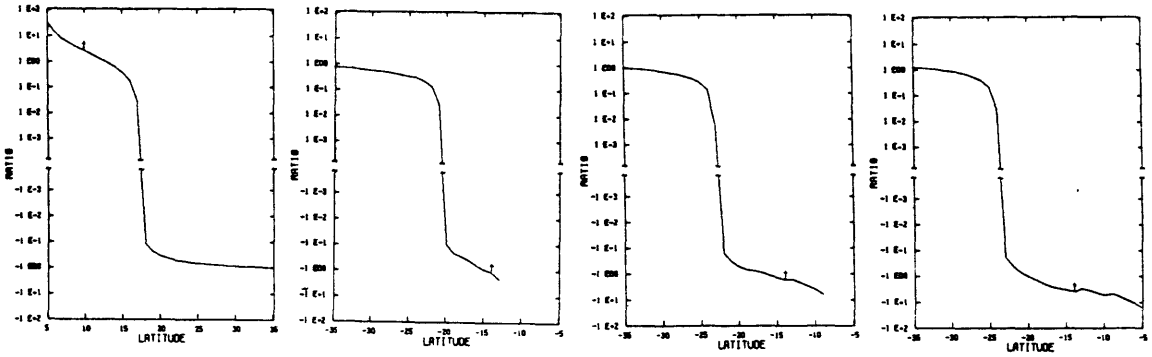

Lat = 4N P = 468 mb du/dy = -8.19×10^{-6} s^{-1}

Lat = 12S P = 468 mb du/dy = -2.27×10^{-5} s^{-1}

Lat = 8S P = 468 mb du/dy = -1.14×10^{-5} s^{-1}

Lat = 4S P = 468 mb du/dy = -4.38×10^{-6} s^{-1}

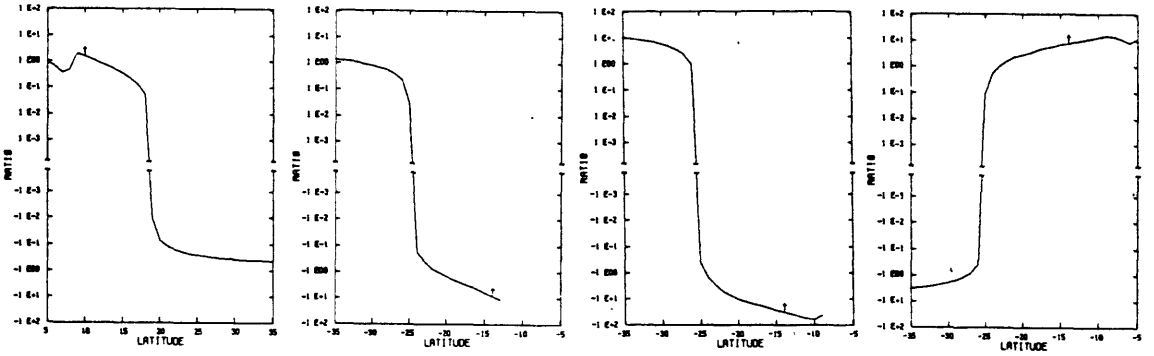

Lat = 4N P = 720 mb du/dy = -1.68×10^{-5} s^{-1}

Lat = 12S P = 720 mb du/dy = -9.84×10^{-6} s^{-1}

Lat = 8S P = 720 mb du/dy = -8.78×10^{-7} s^{-1}

Lat = 4S P = 720 mb du/dy = 1.45×10^{-6} s^{-1}

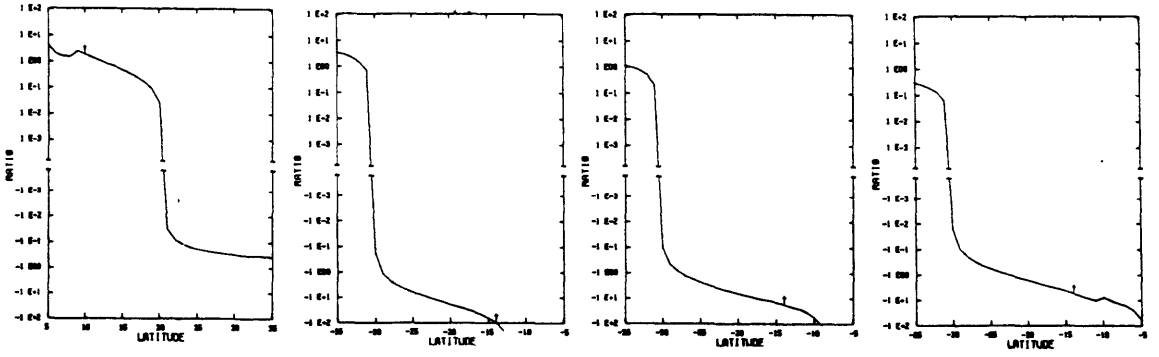

Lat = 4N P = 894 mb du/dy = -1.83×10^{-5} s^{-1}

Lat = 12S P = 894 mb du/dy = 2.30×10^{-6} s^{-1}

Lat = 8S P = 894 mb du/dy = 4.39×10^{-6} s^{-1}

Lat = 4S P = 894 mb du/dy = -9.00×10^{-6} s^{-1}

Figure 3.9 Ratio of theoretically calculated du/dy to numerical value of du/dy as a function of y_0 for run NC1-S1 (leftmost column) and run NC1-S2 (three rightmost columns). Dagger indicates optimum choice of y_0. The latitude and pressure of the calculation, as well as the numerical value of du/dy are listed under each plot.

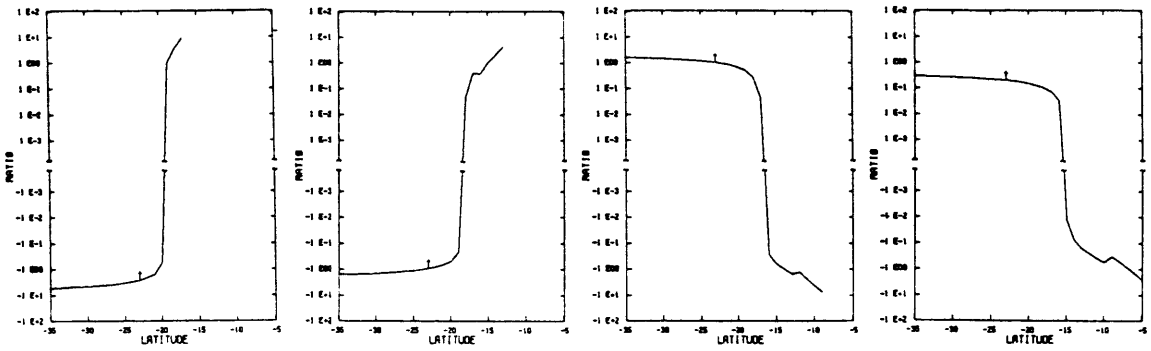

Lat = 16S P = 468 mb
du/dy = 6.12 x 10^{-6} s^{-1}

Lat = 12S P = 468 mb
du/dy = 1.54 x 10^{-5} s^{-1}

Lat = 8S P = 468 mb
du/dy = -1.01 x 10^{-5} s^{-1}

Lat = 4S P = 468 mb
du/dy = -2.81 x 10^{-5} s^{-1}

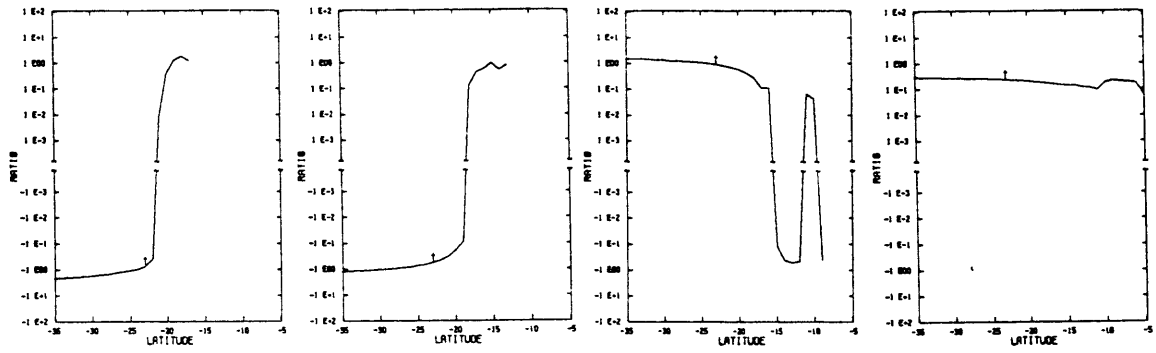

Lat = 16S P = 720 mb
du/dy = 1.36 x 10^{-5} s^{-1}

Lat = 12S P = 720 mb
du/dy = 1.85 x 10^{-5} s^{-1}

Lat = 8S P = 720 mb
du/dy = -1.05 x 10^{-5} s^{-1}

Lat = 4S P = 720 mb
du/dy = -3.05 x 10^{-5} s^{-1}

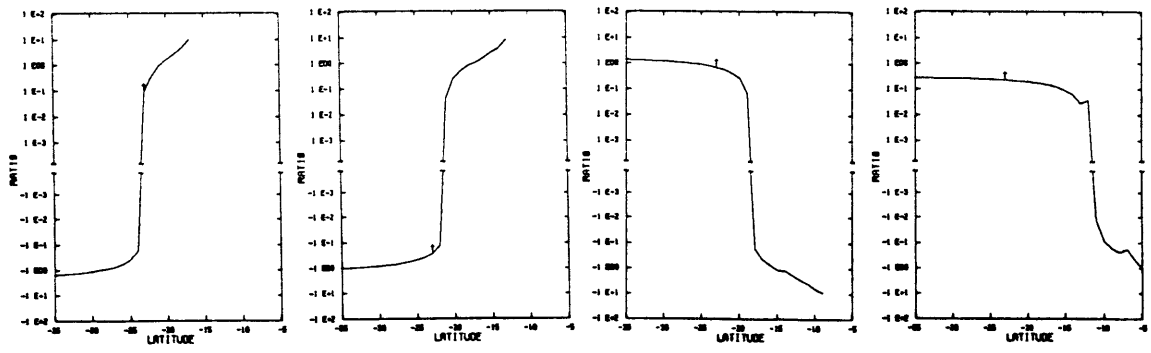

Lat = 16S P = 894 mb
du/dy = 1.74 x 10^{-5} s^{-1}

Lat = 12S P = 894 mb
du/dy = 2.08 x 10^{-5} s^{-1}

Lat = 8S P = 894 mb
du/dy = -1.07 x 10^{-5} s^{-1}

Lat = 4S P = 894 mb
du/dy = -3.18 x 10^{-5} s^{-1}

Figure 3.10 Identical to figure 3.9 except for run MC2-A.

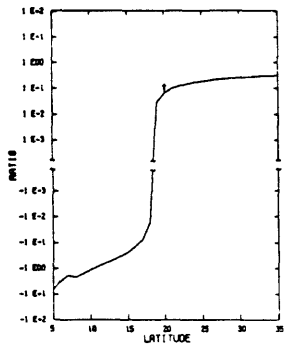

Lat = 4N P = 468 mb
du/dy = 2.46×10^{-5} s^{-1}

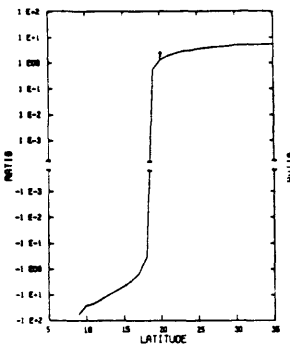

Lat = 8N P = 468 mb
du/dy = 2.80×10^{-6} s^{-1}

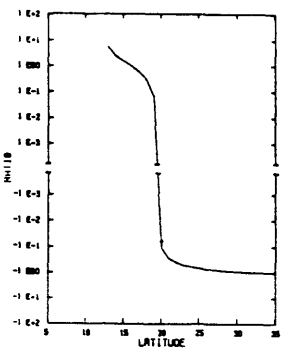

Lat = 12N P = 468 mb
du/dy = -2.25×10^{-5} s^{-1}

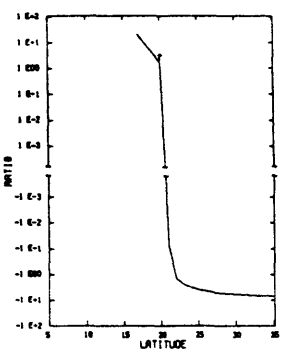

Lat = 16N P = 468 mb
du/dy = -4.68×10^{-6} s^{-1}

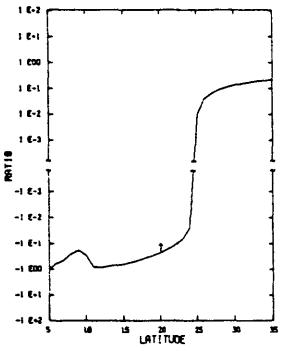

Lat = 4N P = 720 mb
du/dy = 2.33×10^{-5} s^{-1}

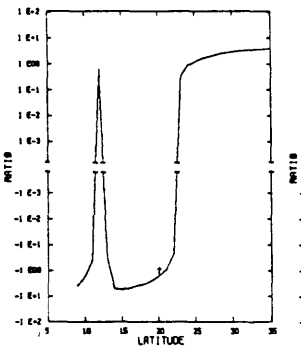

Lat = 8N P = 720 mb
du/dy = 3.04×10^{-6} s^{-1}

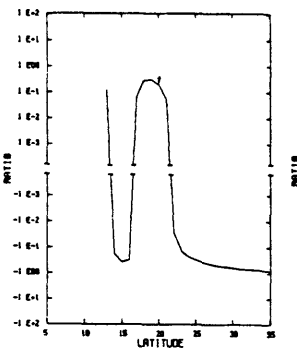

Lat = 12N P = 720 mb
du/dy = -2.34×10^{-5} s^{-1}

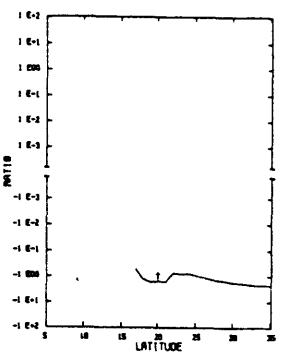

Lat = 16N P = 720 mb
du/dy = -1.10×10^{-5} s^{-1}

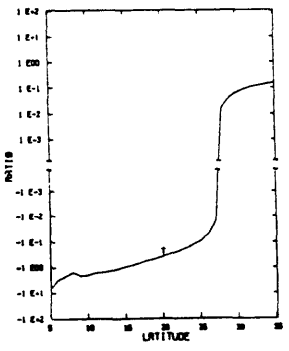

Lat = 4N P = 894 mb
du/dy = 2.42×10^{-5} s^{-1}

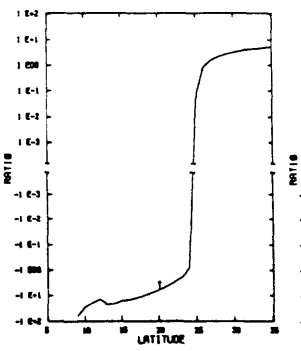

Lat = 8N P = 894 mb
du/dy = 1.99×10^{-6} s^{-1}

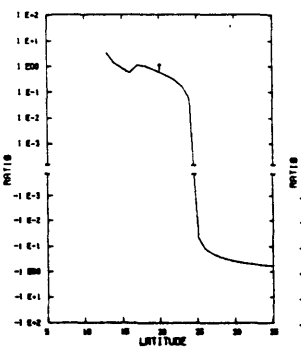

Lat = 12N P = 894 mb
du/dy = -2.76×10^{-5} s^{-1}

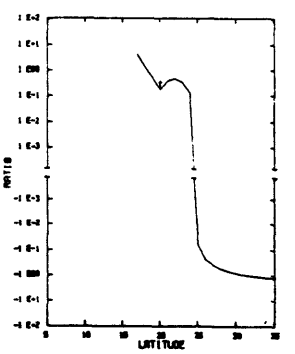

Lat = 16N P = 894 mb
du/dy = -1.69×10^{-5} s^{-1}

Figure 3.11 Identical to figure 3.9 except for run MC2-A (cont'd).

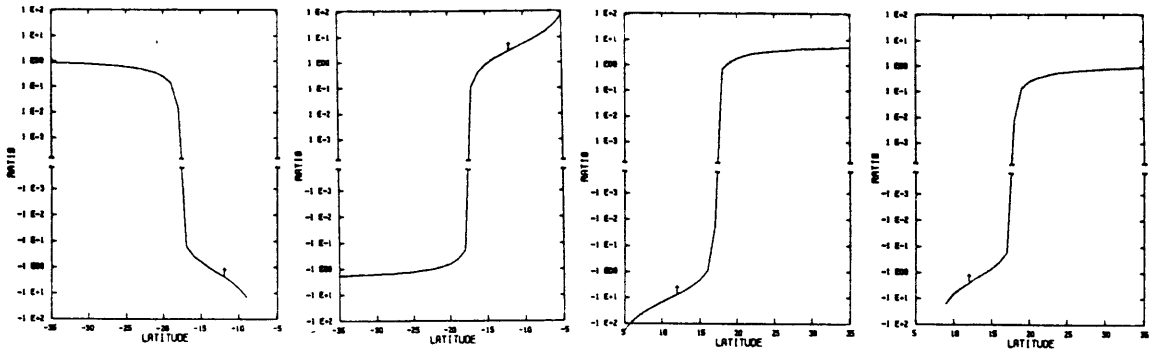

Lat = 8S P = 468 mb du/dy = -1.82×10^{-5} s^{-1}

Lat = 4S P = 468 mb du/dy = 4.38×10^{-6} s^{-1}

Lat = 4N P = 468 mb du/dy = 1.62×10^{-6} s^{-1}

Lat = 8S P = 468 mb du/dy = 1.81×10^{-5} s^{-1}

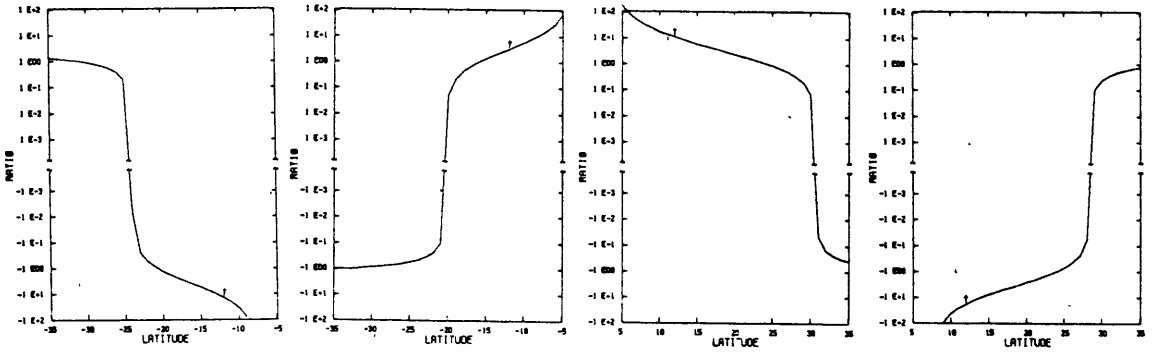

Lat = 8S P = 720 mb du/dy = 8.90×10^{-6} s^{-1}

Lat = 4S P = 720 mb du/dy = 7.01×10^{-6} s^{-1}

Lat = 4N P = 720 mb du/dy = -6.43×10^{-6} s^{-1}

Lat = 8N P = 720 mb du/dy = 1.01×10^{-5} s^{-1}

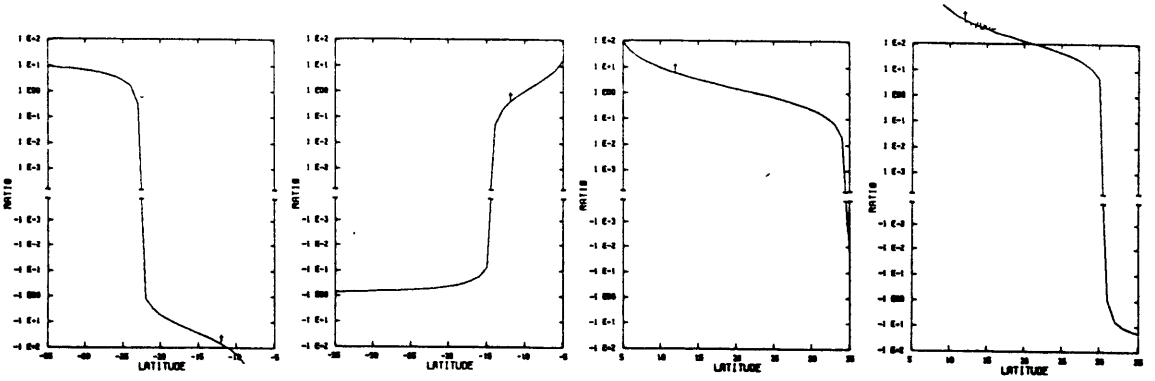

Lat = 8S P = 894 mb du/dy = -1.46×10^{-6} s^{-1}

Lat = 4S P = 894 mb du/dy = 1.28×10^{-5} s^{-1}

Lat = 4N P = 894 mb du/dy = -1.59×10^{-5} s^{-1}

Lat = 8N P = 894 mb du/dy = -2.68×10^{-7} s^{-1}

Figure 3.12 Identical to figure 3.9 except for run MD-A.

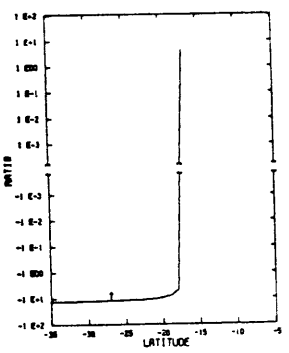

Lat = 16S P = 468 mb
du/dy = 2.98 x 10^{-6} s^{-1}

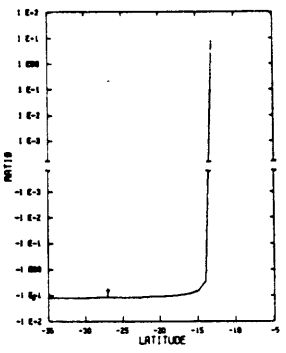

Lat = 12S P = 468 mb
du/dy = 2.32 x 10^{-6} s^{-1}

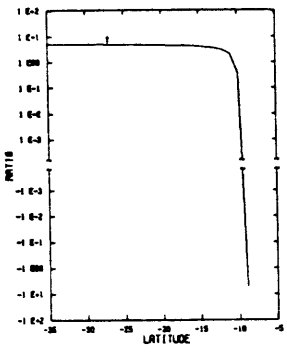

Lat = 8S P = 468 mb
du/dy = -3.90 x 10^{-6} s^{-1}

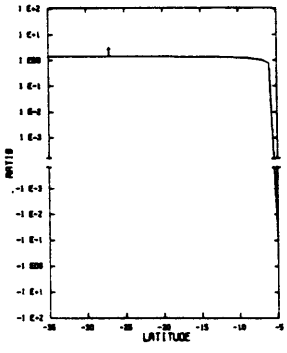

Lat = 4S P = 468 mb
du/dy = -7.15 x 10^{-6} s^{-1}

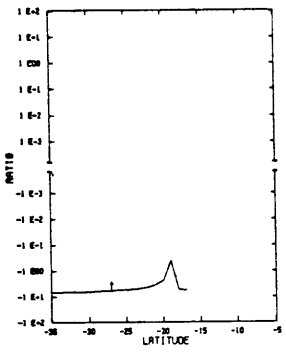

Lat = 16S P = 720 mb
du/dy = 5.28 x 10^{-6} s^{-1}

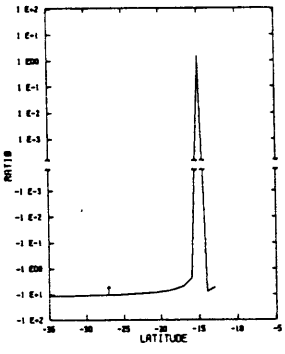

Lat = 12S P = 720 mb
du/dy = 2.42 x 10^{-6} s^{-1}

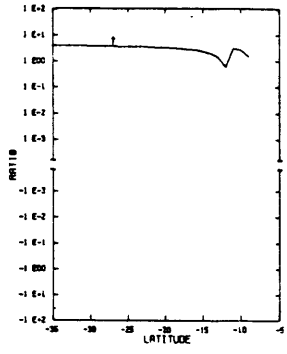

Lat = 8S P = 720 mb
du/dy = -4.63 x 10^{-6} s^{-1}

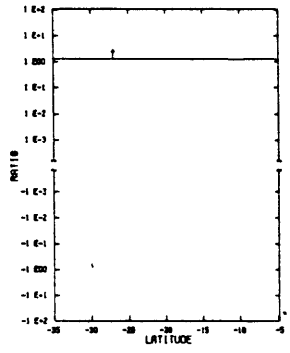

Lat = 4S P = 720 mb
du/dy = -7.82 x 10^{-6} s^{-1}

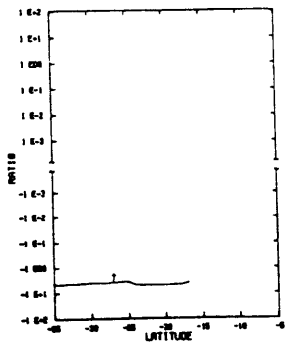

Lat = 16S P = 894 mb
du/dy = 7.35 x 10^{-6} s^{-1}

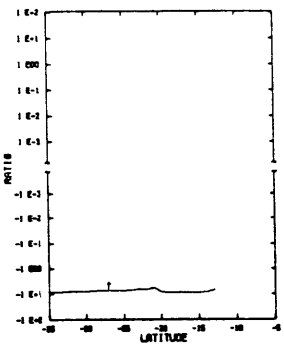

Lat = 12S P = 894 mb
du/dy = 3.12 x 10^{-6} s^{-1}

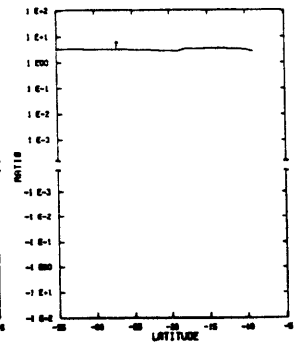

Lat = 8S P = 894 mb
du/dy = -5.50 x 10^{-6} s^{-1}

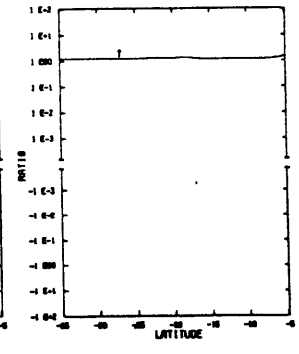

Lat = 4S P = 894 mb
du/dy = -9.23 x 10^{-6} s^{-1}

Figure 3.13 Identical to figure 3.9 except for run MC1-A.

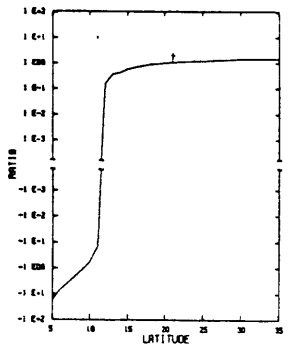

Lat = 4N P = 468 mb
du/dy = 5.65 x 10^{-6} s^{-1}

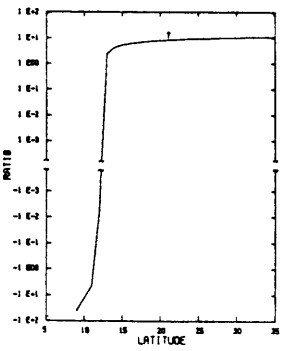

Lat = 8N P = 468 mb
du/dy = 1.64 x 10^{-6} s^{-1}

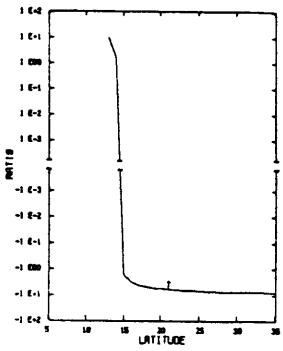

Lat = 12N P = 468 mb
du/dy = -3.59 x 10^{-6} s^{-1}

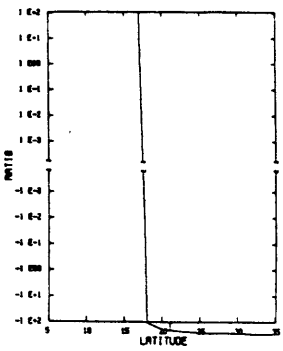

Lat = 16N P = 468 mb
du/dy = -1.25 x 10^{-7} s^{-1}

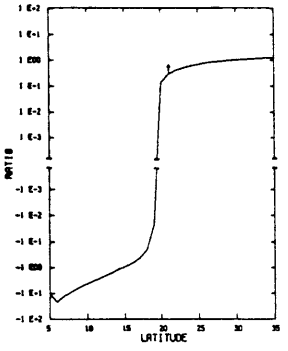

Lat = 4N P = 720 mb
du/dy = 5.39 x 10^{-6} s^{-1}

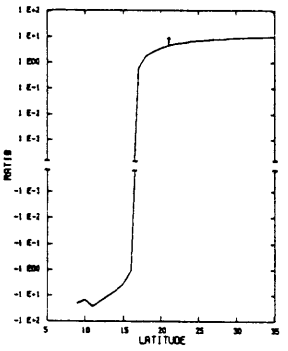

Lat = 8N P = 720 mb
du/dy = 1.51 x 10^{-6} s^{-1}

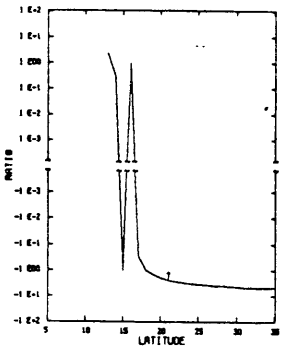

Lat = 12N P = 720 mb
du/dy = -4.93 x 10^{-6} s^{-1}

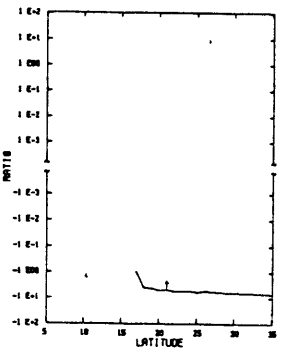

Lat = 16N P = 720 mb
du/dy = -4.64 x 10^{-6} s^{-1}

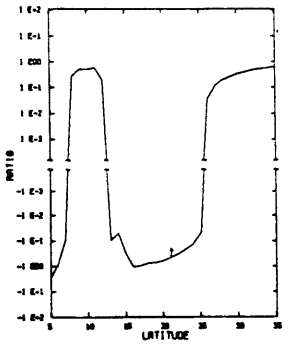

Lat = 4N P = 894 mb
du/dy = 6.23 x 10^{-6} s^{-1}

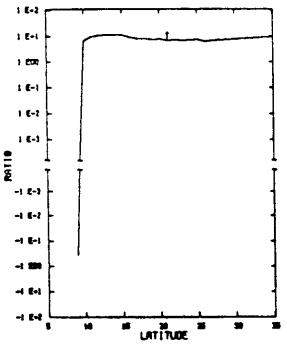

Lat = 8N P = 894 mb
du/dy = 1.23 x 10^{-6} s^{-1}

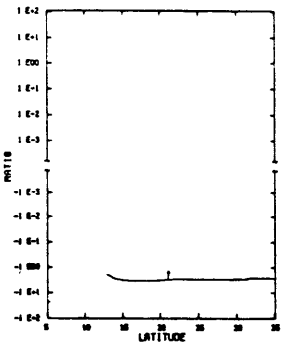

Lat = 12N P = 894 mb
du/dy = -7.39 x 10^{-6} s^{-1}

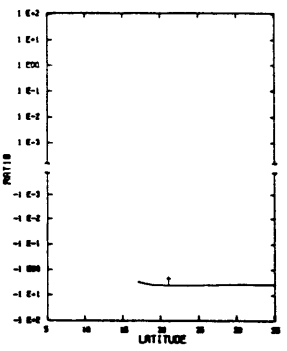

Lat = 16N P = 894 mb
du/dy = -8.74 x 10^{-6} s^{-1}

Figure 3.14 Identical to figure 3.9 except for run MC1-A (cont'd).

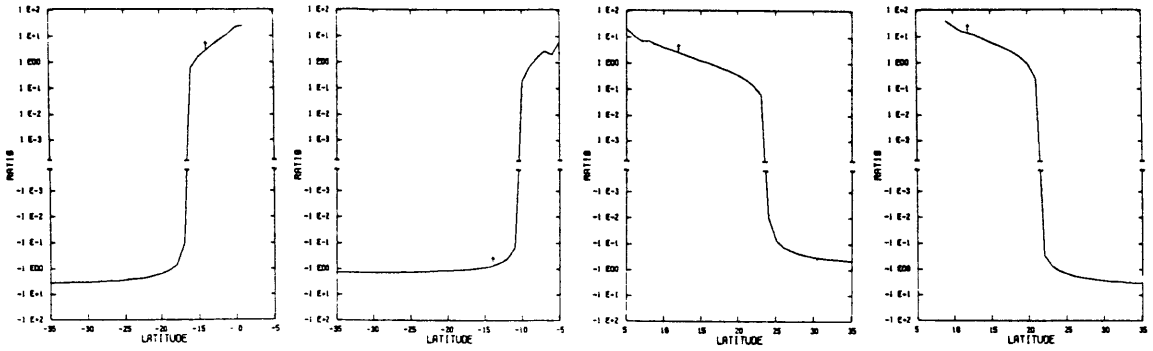

Lat = 8S P = 468 mb
du/dy = 4.67 x 10^{-6} s^{-1}

Lat = 4S P = 468 mb
du/dy = 6.92 x 10^{-6} s^{-1}

Lat = 4N P = 468 mb
du/dy = -1.25 x 10^{-5} s^{-1}

Lat = 8S P = 468 mb
du/dy = -3.88 x 10^{-6} s^{-1}

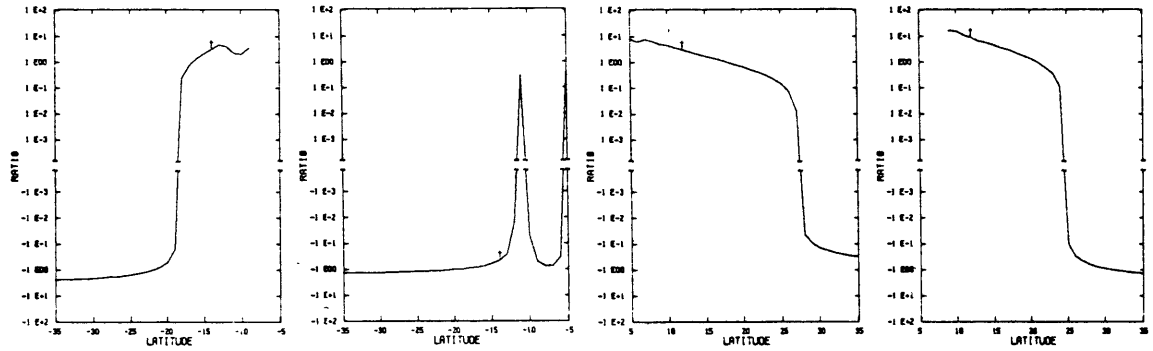

Lat = 8S P = 720 mb
du/dy = 6.67 x 10^{-6} s^{-1}

Lat = 4S P = 720 mb
du/dy = 6.78 x 10^{-6} s^{-1}

Lat = 4N P = 720 mb
du/dy = -1.30 x 10^{-5} s^{-1}

Lat = 8N P = 720 mb
du/dy = -7.98 x 10^{-6} s^{-1}

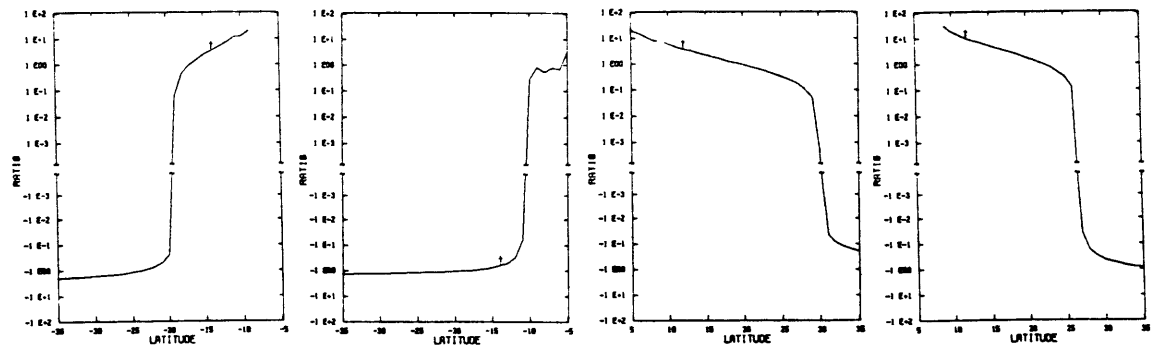

Lat = 8S P = 894 mb
du/dy = 7.84 x 10^{-6} s^{-1}

Lat = 4S P = 894 mb
du/dy = 7.27 x 10^{-6} s^{-1}

Lat = 4N P = 894 mb
du/dy = -1.43 x 10^{-5} s^{-1}

Lat = 8N P = 894 mb
du/dy = -1.02 x 10^{-5} s^{-1}

Figure 3.15 Identical to figure 3.9 except for run NC1-A.

Figure 3.12 shows the results for run MD-A. In this run either the sign of the theoretically calculated value is opposite to that of the data-calculated value, or the calculated value is much too large. At low levels and latitudes where the sign is opposite, however, the data-calculated values of du/dy have a sign inconsistent with that required by Ekman pumping theory. Recall that run MD-A had no moist convection parameterization scheme and virtually no visible congruence between its S^* and M fields (see figure 3.2d).

The results for run MC1-A are shown in figures 3.13 and 3.14. As in run MC2-A, the region from the equator to 6N is actually one of weak descent. The results for 4N are included for comparison with those from the other latitudes. Negative ratios at the two most poleward latitudes in either hemisphere indicate a lack of sign agreement between theoretically and data-calculated values of du/dy. Unlike the previous runs, however, in this case the theoretically calculated values of du/dy at low levels have a sign inconsistent with that from Ekman pumping theory. At the three innermost latitudes in the ascent region, the theoretically calculated values are remarkably constant. When these values were further separated into the ßy-term and the dS^*/dy term, however, the ßy-term dominated by at least an order of magnitude. This is not surprising though, considering the weak meridional gradient of saturated moist entropy present in this run.

Finally, figure 3.15 shows the results for run NC1-A. Positive ratios in the ascent regions indicate good sign agreement between theoretically and data-calculated values of du/dy

everywhere except at 4S at 720 mb. This is true even at 4S (at the other levels) despite the fact that the region from the equator to 6S is one of weak descent. Also, at low levels the signs are consistent with Ekman pumping theory. Even though the theoretically calculated values are not very constant in the ascent region, they are within an order of magnitude of the data-calculated values. The better agreement in this run is probably attributable to the constraint of no momentum mixing, and hence more congruence between the S^* and M fields.

In summary, it is apparent that none of the cases indicate a complete verification of the vorticity prediction. Those cases that indicate a qualitative verification are those whose theoretically calculated values of du/dy are within an order of magnitude of the data-calculated ones, have the same sign, and are quasi-constant within ascent regions. Thus, only in runs NC1-S1 and NC1-A is the vorticity prediction qualitatively verified, as well as at the two southernmost latitudes in either hemisphere of run MC2-A. The quasi-constant values may be explainable by the fact that the theoretically calculated values of du/dy are, in most cases, residuals of two larger numbers. The degree of verification does not appear to be dependent on the level of calculation. In those cases showing qualitative verification, this may be an indication that processes working in the troposphere responsible for the violation of those assumptions leading up to the vorticity prediction are the same and/or of equivalent influence throughout.

3.7 Vertical Velocity and Sea Surface Temperature

The second major prediction of the theory implied by Eq. (18) was that a maximum in vertical velocity at the top of the PBL should exist equatorward of a minimum (maximum) in the meridional SST gradient in the northern (southern) hemisphere. This was investigated qualitatively and the results are shown graphically in Figure 3.16. In this figure, the model vertical velocities at 894 mb and the corresponding SST distributions are shown for all the runs. The model vertical velocities instead of the calculated Ekman velocities are compared to the SST distributions to examine the verification of this prediction independently from the validity of the assumptions leading up to this prediction.

The results can be broken up into two groups: the first group consisting of those runs having a double ITCZ and the second group consisting of those runs having a single ITCZ. Those runs indicating a double ITCZ also have asymmetric SST distributions with a broad maximum from 12S to 4N. Despite the meridionally asymmetric forcing in runs MC2-A and MC1-A, the vertical velocity profiles are somewhat meridionally symmetric, considering the coarse resolution of the data. Run NC1-A indicates a much less meridionally symmetric velocity profile. For these three runs, the maxima in the velocity profiles are located on either side of the broad maximum in SST, although this is more evident for runs MC2-A and MC1-A. Although the plotted data is from 27S to 27N, it should be noted for all the runs that the magnitudes of the meridional SST gradients were even larger at more poleward latitudes. Hence, the vertical velocity maxima are indeed located

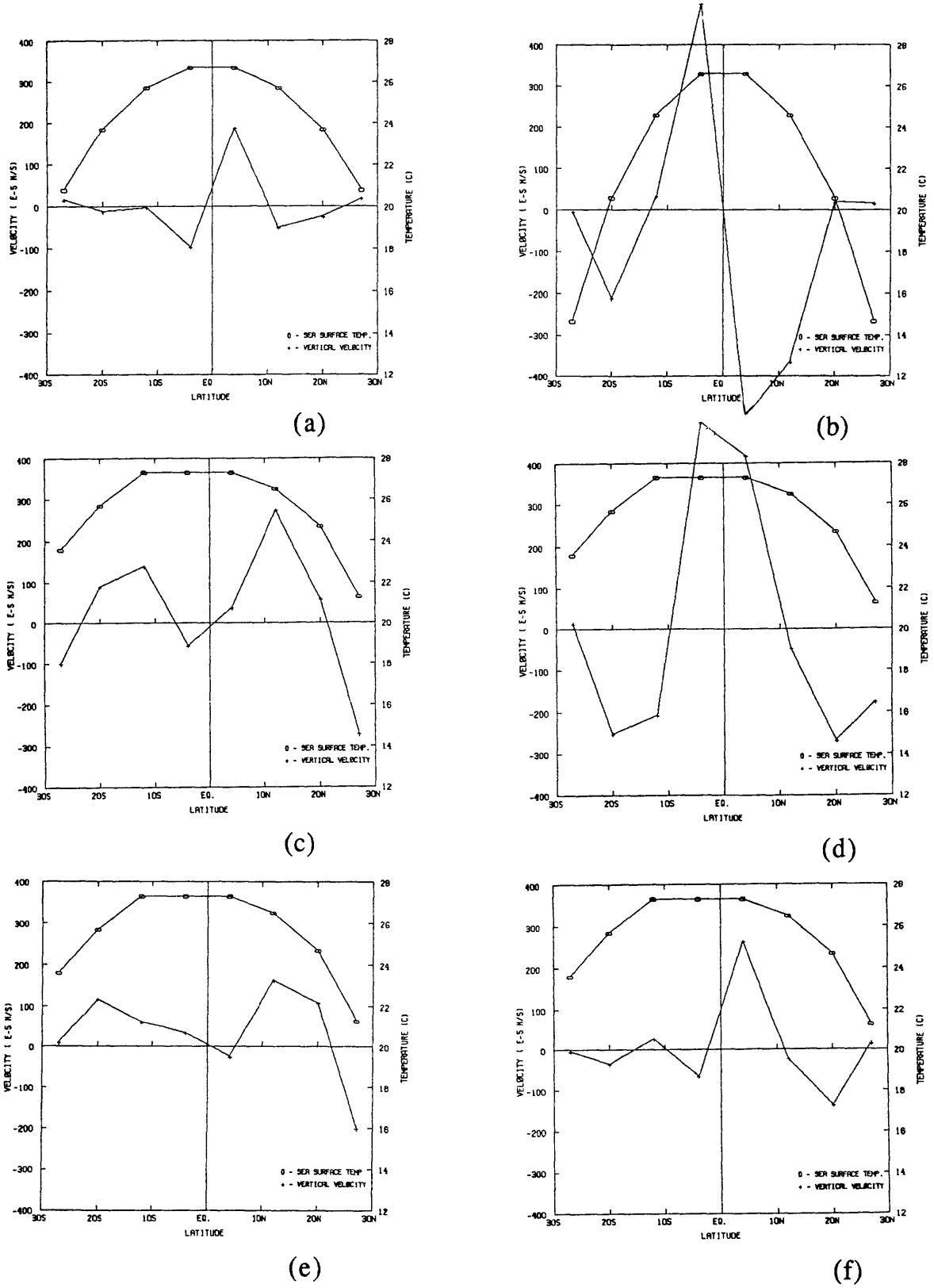

Figure 3.16 Model vertical velocities (+) at 854 mb and sea surface temperatures (0) for the six 2-D model runs: (a) NC1-S1, (b) NC1-S2, (c) MC2-A, (d) MD-A, (e) MC1-A, and (f) NC1-A.

equatorward of the extrema in the meridional SST gradients. The results for run NC1-S1 are somewhat puzzling considering this run had meridionally symmetric forcing in all aspects; nevertheless it indicates a very asymmetric vertical velocity distribution. Runs NC1-S2 and MD-A show unrealistically large vertical velocity magnitudes. This can be explained from the unrealistic conditions of no moist convection in run MD-A and exceptionally large meridional SST gradients in run NC1-S2. The results from run MD-A when compared to those from runs MC2-A and MC1-A indicate the dependence of a double ITCZ on the presence of moist convection. The results from NC1-S2 when compared to those from NC1-S1 indicate the dependence of vertical velocity magnitudes on the size of meridional SST gradients.

In summary, it is difficult to assess the validity of the prediction that a vertical velocity maximum is located equatorward of a minimum (maximum) in the meridional gradient of SST in the northern (southern) hemisphere for two reasons. The first reason is that even for those runs indicating double ITCZ structures, the fact that the magnitudes of the meridional SST gradients increase away from the equator screens the determination of a correlation between the two fields; i.e. the vertical velocity maxima could be located much more poleward and the prediction might still appear valid. The second reason is that run NC1-S1, which was the most symmetric run, did not indicate a meridionally symmetric vertical velocity distribution.

CHAPTER IV

THREE-DIMENSIONAL DATA ANALYSIS

4.1 Data Description

The data for analysis in this section was obtained on magnetic tape from the GFDL Atmospheric Circulation Tape Library. The data consisted of ten-year (May 1963 to April 1973) monthly mean analyses of zonal wind (u), meridional wind (v), temperature (T), and specific humidity (q) at eleven pressure levels. The levels included 1000 mb, 950 mb, 900 mb, 850 mb, 700 mb, 500 mb, 400 mb, 300 mb, 200 mb, 100 mb, and 50 mb. The horizontal spacing for the grid data was 2.5° latitude and 5.0° longitude. Unfortunately, vertical velocity data was not available. Further information about this data set can be found in Oort (1983).

Another data set containing sea-surface temperature (SST) data was also obtained from Rodger Parker (personal communication, 1986). This set included thirty-year (1949 to 1979) monthly mean analyses of sea surface temperature every 5.0° latitude and every 5.0° longitude for both the Atlantic and Pacific Oceans. A cubic-spline was applied to this data set in the latitudinal direction for the purpose of conforming to the horizontal resolution of the other data set.

4.2 Selection of Regions

The selection of regions for study was based mainly upon visible inspection of satellite photographs of cloud cover in the tropics for various times of the year. It was presupposed that a

region exhibiting a double ITCZ (visible on satellite photographs as a double-banded cloud structure near the equator) would be a region relevant for study, particularly if the bands were on opposite sides of the equator. The reason for this is that some of the symmetry required by the theory would be present in this region. Regions were also examined for zonal uniformity, i.e. regions where zonal derivatives of the various quantities was small compared to meridional derivatives of the various quantities. This was important for obtaining a feasible zonal average across the region. Hence, regions adjacent to large land masses on the windward side in the tropics were excluded from consideration.

Based on the above selection criteria, data from the region 145W to 175W were selected for analysis. Satellite photographs showed a double ITCZ in this area at certain times during the months of April and October. Preliminary calculations at low levels for this region for these two months indicated that S^* distributions were not meridionally symmetric near the equator. Thus for comparison purposes, two other regions while not exhibiting double ITCZ's but more meridionally symmetric S^* distributions at low levels for the months of April and October instead, were also selected for analysis. The region from 175E to 155E (henceforth referred to as region I) and the region from 125W to 145W (henceforth referred to as region III), in conjunction with region II (145W to 175W), thus account for most of the Pacific Ocean. No regions in the Atlantic were found to have sufficient zonal symmetry to warrant selection. (The asymmetry found in the equatorial regions of the Atlantic are due mainly to the presence of

the Sahara Desert to the East.) For additional comparison, regions I, II, and III were examined for the months of January, April, July, and October. Investigation of the regions for January and July conditions allowed the theory to be tested under more meridionally asymmetric conditions.

4.3 Analysis of S^* and M Fields

Before proceeding, the zonal averaging method used not only for these calculations but for all subsequent ones in this section is summarized. For a given region, the zonal average of a field at a particular latitude was taken as the mean of the values for that field for all longitudes within that region. Further calculations involving differentiation were then performed on this new, quasi-zonally averaged data set.

The first assumption which was invstigated was the validity of that stated in equation (10), i.e. that S^* and M fields are congruent above the top of the PBL. The validity of this assumption was again first qualitatively determined by examining the cross-sectional profiles of the regions' S^* and M fields. Figures 4.1 and 4.2 are the 3-D data counterparts to figure 3.2, showing the S^* field calculated for a LCL at 900 mb. Generally, it is not difficult to note a lack of congruence between the two fields in tropical latitudes, despite an absence of sufficient resolution of the S^* field at these latitudes. This incongruity appears more pronounced in summer hemispheres, less pronounced in winter hemispheres, and less pronounced in all three regions during the transition months, particularly April.

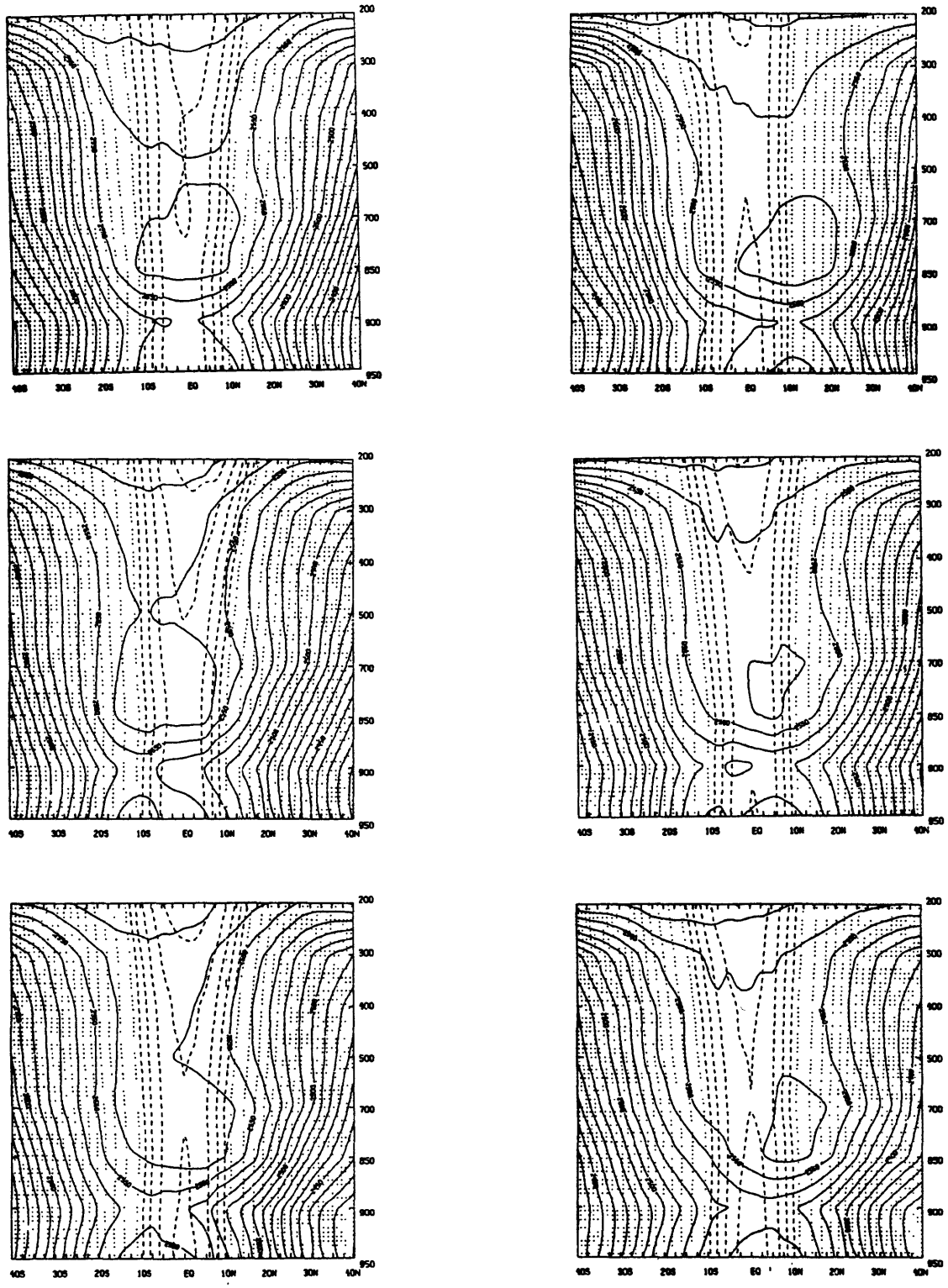

Column A Column B

Figure 4.1 Latitude-pressure contour plots of saturated moist entropy (solid lines, interval is 10 J/kgK) with LCL = 900 mb and M (dotted (contour interval is 10 m^2/s) and dashed (contour interval is 4 m^2/s) lines) for region I (upper), region II (middle), and region III (lower) for April (column A) and October (column B).

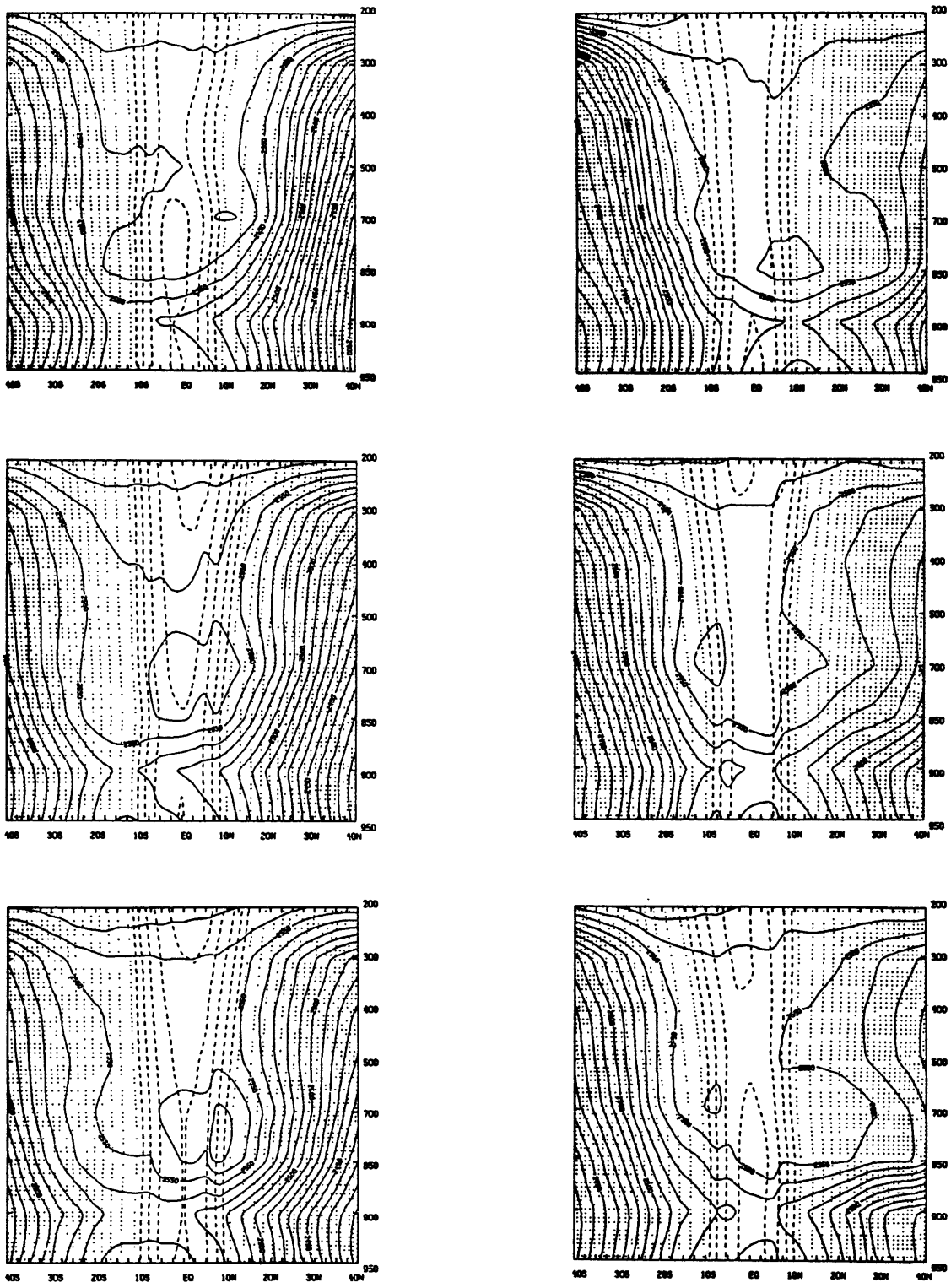

Column A Column B

Figure 4.2 Identical to figure 4.1 except for January (column A) and July (column B).

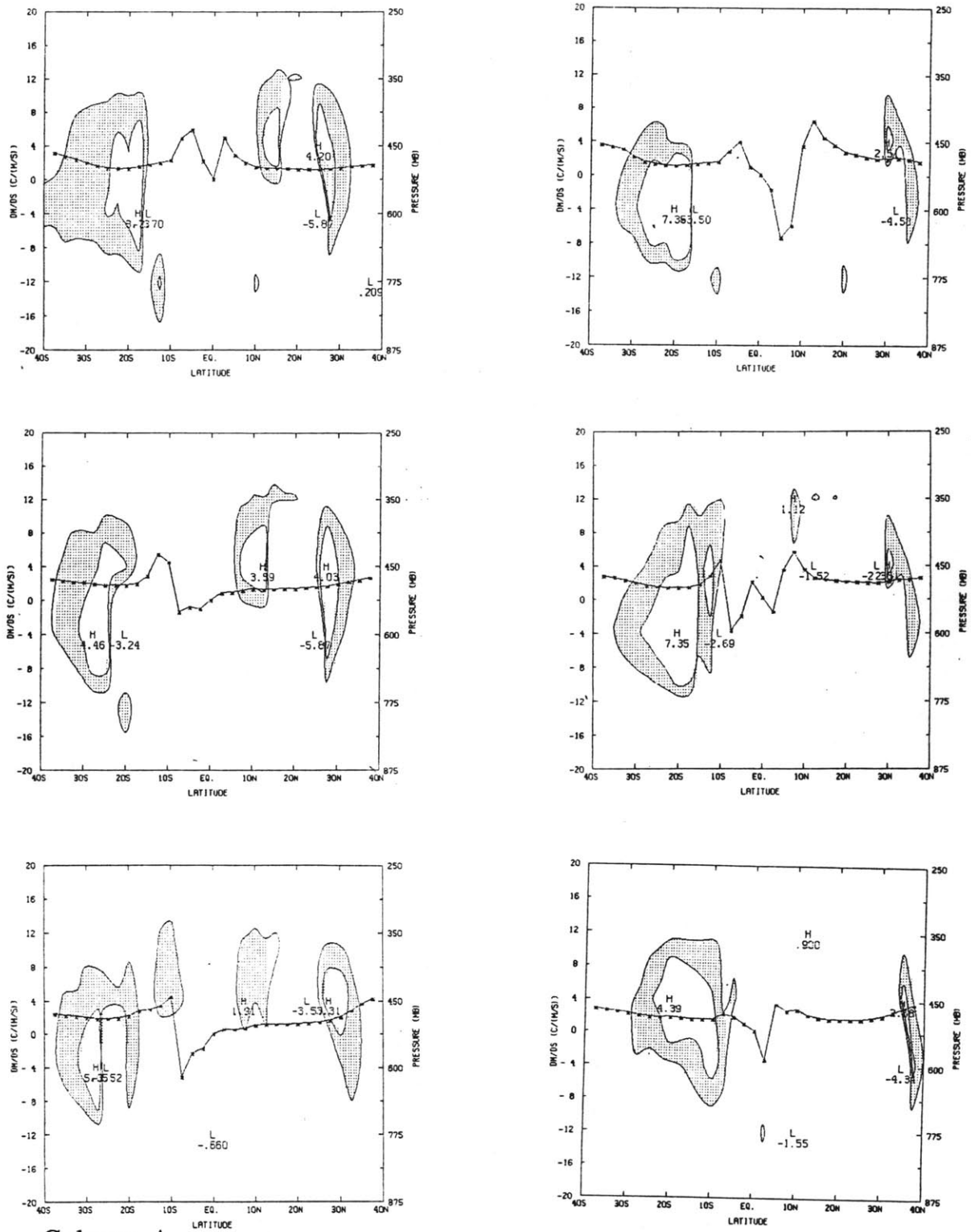

Column A Column B

Figure 4.3 Profiles of dM/dS^* (*) calculated in the y-direction at 900 mb and latitude-pressure contour plots of dM/dS^* calculated in the P-direction for region I (upper), region II (middle), and region III (lower) for April (column A) and October (column B). Shading indicates values between 1.0 and 2.0 °C/(m/s).

The validity of this assumption was then investigated more quantitatively. A procedure similar to that used to examine the 2-D model data was used to compare dM/dS^* calculated in the y-direction along the top of the PBL (900 mb) with dM/dS^* calculated in the P-direction throughout the troposphere. The results are shown in figure 4.3. The contoured areas indicate regions of dM/dS^* calculated in the P-direction with values between 1.0 and 2.0 K/(m/s). The superimposed asterisked line shows the corresponding values for dM/dS^* calculated in the y-direction at 900 mb as a function of latitude. The vertical scale on the left hand side corresponds to this graph.

Only April and October are shown for the three regions, as the other two months show qualitatively similar results. The common features include very isolated areas located in the middle troposphere where values are near those calculated at 900 mb and in the y-direction. Most of each cross-section indicates smaller (in magnitude) or negative values of dM/dS^* calculated in the P-direction than those obtained at 900 mb in the y-direction. A measure of the congruence is that the contoured regions have values near those calculated at the top of the PBL in the y-direction with the contour lines themselves being flared in a manner similar to those of either the S^* or M fields. Ideally congruent fields will have dM/dS^* equal to a constant along an isentrope or constant M line regardless of the direction in which the derivative is calculated. Hence, the the extremely different values for dM/dS^* as a result of the different directions is a quantitative indication of the incongruity between the S^* and M fields.

With the exception of certain regions where dS^*/dy was very small, the asterisked profiles indicated, as in the 2-D model data set, that dM/dS^* was constant with latitude. This constant-valuedness again prompted further investigation for a possible correlation between the S^* and M fields. Further pursuit of this, however, revealed only that dM/dy was dominated by the βy term, particularly at higher latitudes, and hence linear with latitude. This only reinforced the concept that the saturated moist entropy profile was quadratic. The spikes near the equator are probably due to errors in the data, since a quick sensitivity calculation showed that an error in temperature of only 0.1°C can lead to a 'noisy' computation of dM/dS^* in a region where $\Delta S^* < 3$ J/(kgK) .

While inspection of Figures 4.1 - 4.3 revealed that both S^* and M are not congruent fields, it did not reveal the degree to which either one of the quantities was not conserved or if one quantity was conserved and the other one was not. Assessment of the degrees of non-conservation is important for determining the reasons and processes responsible for the invalidity of the assumption. A straightforward method for determining degrees of conservation would be to examine the superposition of streamlines with lines of constant S^* and constant M for a given region, as was done in the previous section. Hence, mass streamfunctions for each region, Φ_M, were computed according to

$$\Phi_M = \int_{P_0}^{P} \frac{[v]}{g} dP \ ,$$

where P_0 = 1000 mb,

P = pressure at which Φ_M was determined,

[v] = quasi-zonally averaged meridional velocity,

g = 9.8 m/s^2,

and the boundary conditions that Φ_M vanishes at both p = 50 mb (top) and p = 1000 mb (surface). For each pressure interval dP, (approximated as ΔP) the meridional velocity was taken as the vertically averaged mean, using values at the top and bottom of the interval. These computations, however, proved inaccurate despite the regions' quasi-two dimensional structures. The inaccuracies are most likely attributable to erroneous meridional velocity data, particularly at higher levels, since typical magnitudes were relatively small: 1 to 2 m/s. Hence, it is difficult to assess conservation of either of the quantities by comparison of streamlines with isentropes or with constant M lines, as was done in the previous section.

4.4 Ekman Velocity

The second major assumption that was investigated with the 3-D data set was that the vertical velocity at the top of the PBL was equal to the Ekman velocity :

$$w_E = -\left(\frac{du}{dy}\right)\frac{|f|}{f}\sqrt{\frac{K}{2|f|}} \qquad (16)$$

at 900 mb. Obviously, the Ekman velocities could not be calculated

at the equator (f = 0) so that value was determined as the mean of the two adjacent values. For simplicity, and also because surface pressure variations were unknown (and hence it was difficult to determine surface Θ values), the value for K, the eddy viscosity coefficient, was taken as a constant corresponding to stable conditions: 1.0 m^2/s. This assumption did not change the results qualitatively (i.e. the sign of w_E) in the regions of interest, i.e. the ascent regions.

Since vertical velocity data was unobtainable, the actual vertical velocities at 900 mb were obtained through integration of the continuity equation :

$$\left[\frac{\partial u}{\partial x}\right] + \frac{\partial [v]}{\partial y} + \left[\frac{\partial \omega}{\partial P}\right] = 0 \ . \qquad (24)$$

The meridional velocities were first averaged zonally across a region and then differentiated. Values for $[\partial u/\partial x]$ were obtained by taking the difference in zonal velocities between both ends of a region for each latitude. The boundary condition was that $\omega = 0$ at P = 1000 mb.

Figures 4.4 - 4.6 show a comparison of the actual vertical velocities to those calculated based on the Ekman assumption. The four frames in each figure correspond to the four months for each region. As a check on the magnitudes of the vertical velocities calculated using the continuity equation, it can be seen that they are comparable to those found in the 2-D model runs. Comparing the results for the different longitudinal regions, it can be seen that

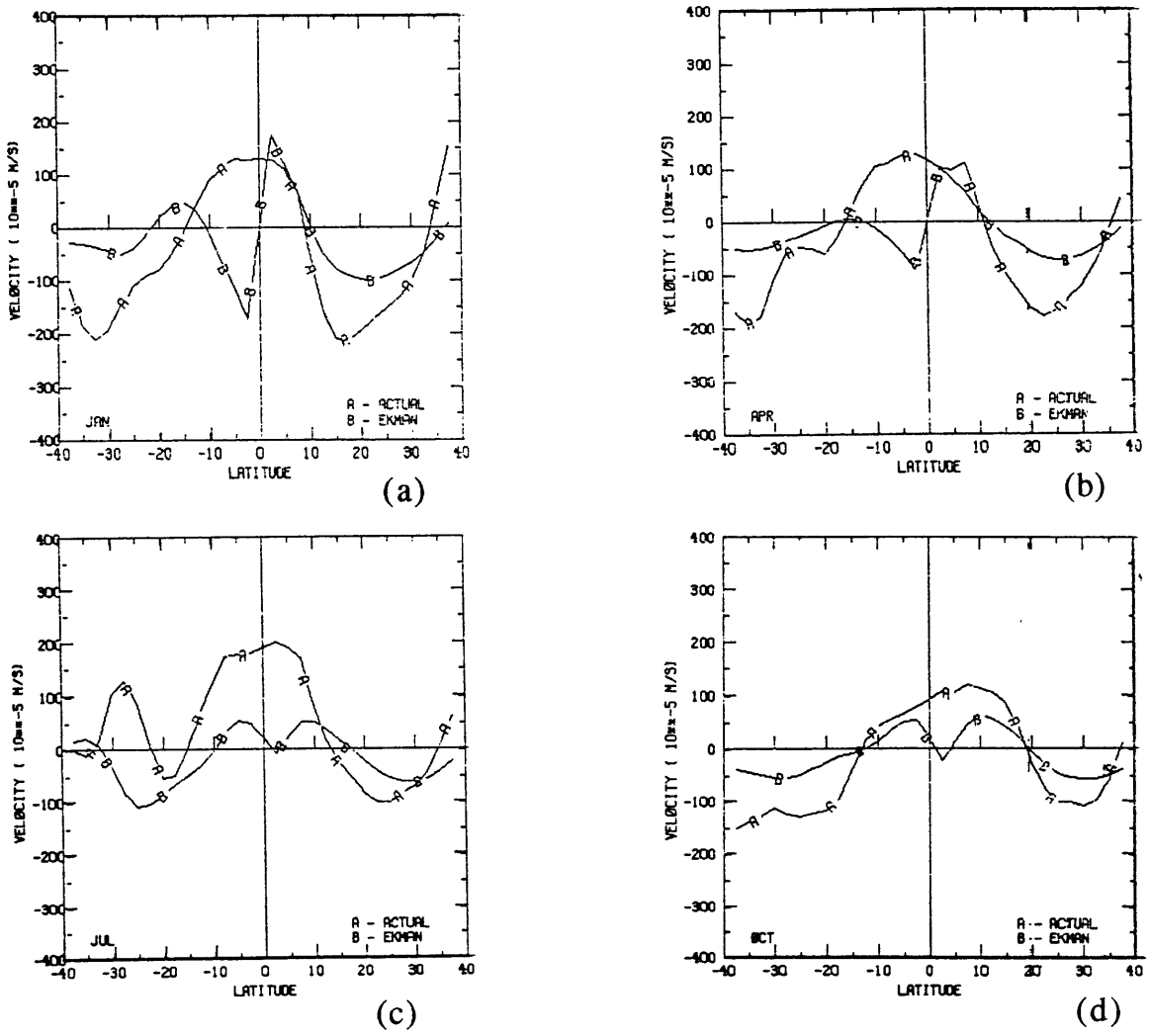

Figure 4.4 Calculated Ekman vertical velocities at 900 mb (B) and actual vertical velocities (A) obtained from integration of Eq. (24) for region I for (a) January, (b) April, (c) July, and (d) October.

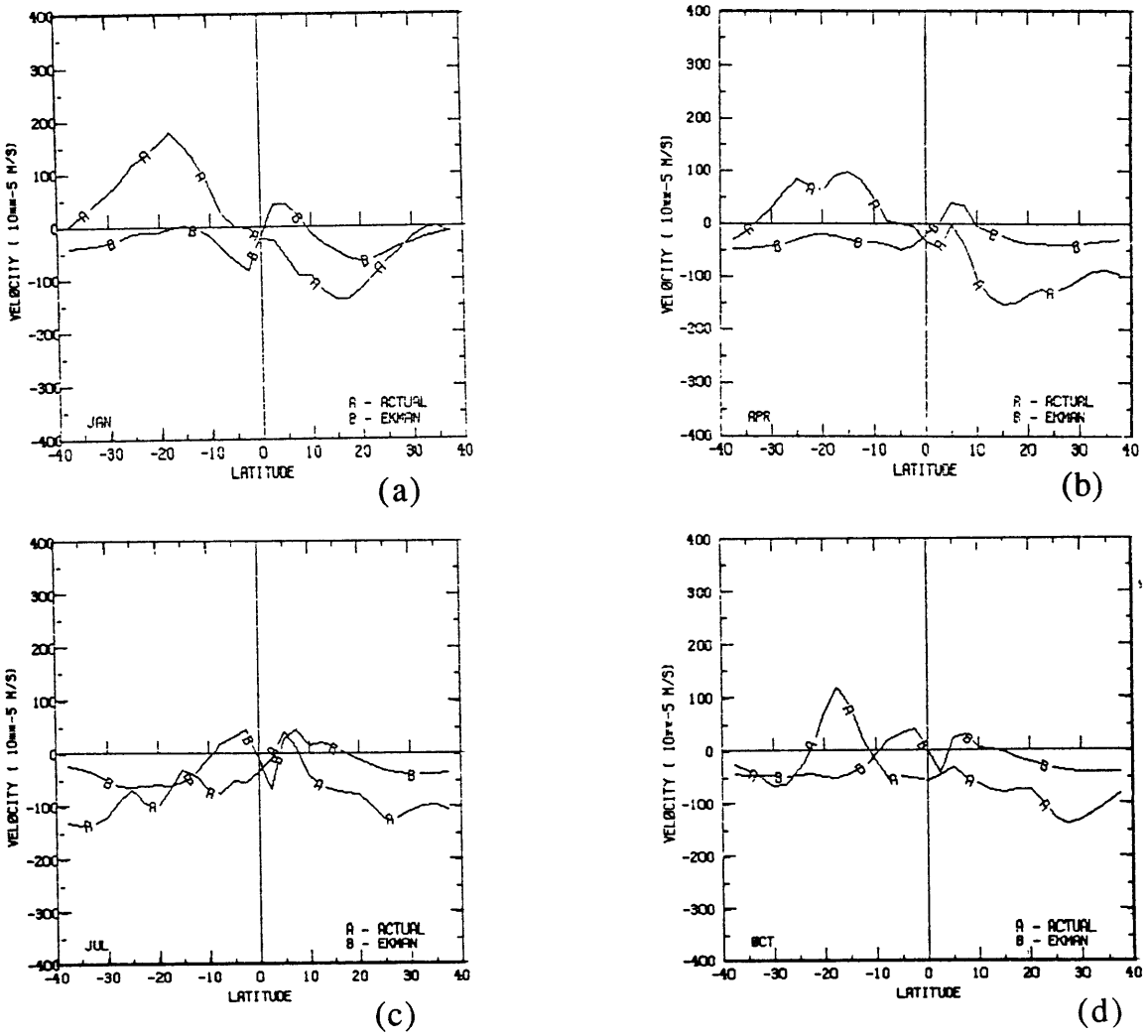

Figure 4.5 Identical to figure 4.4 except for region II.

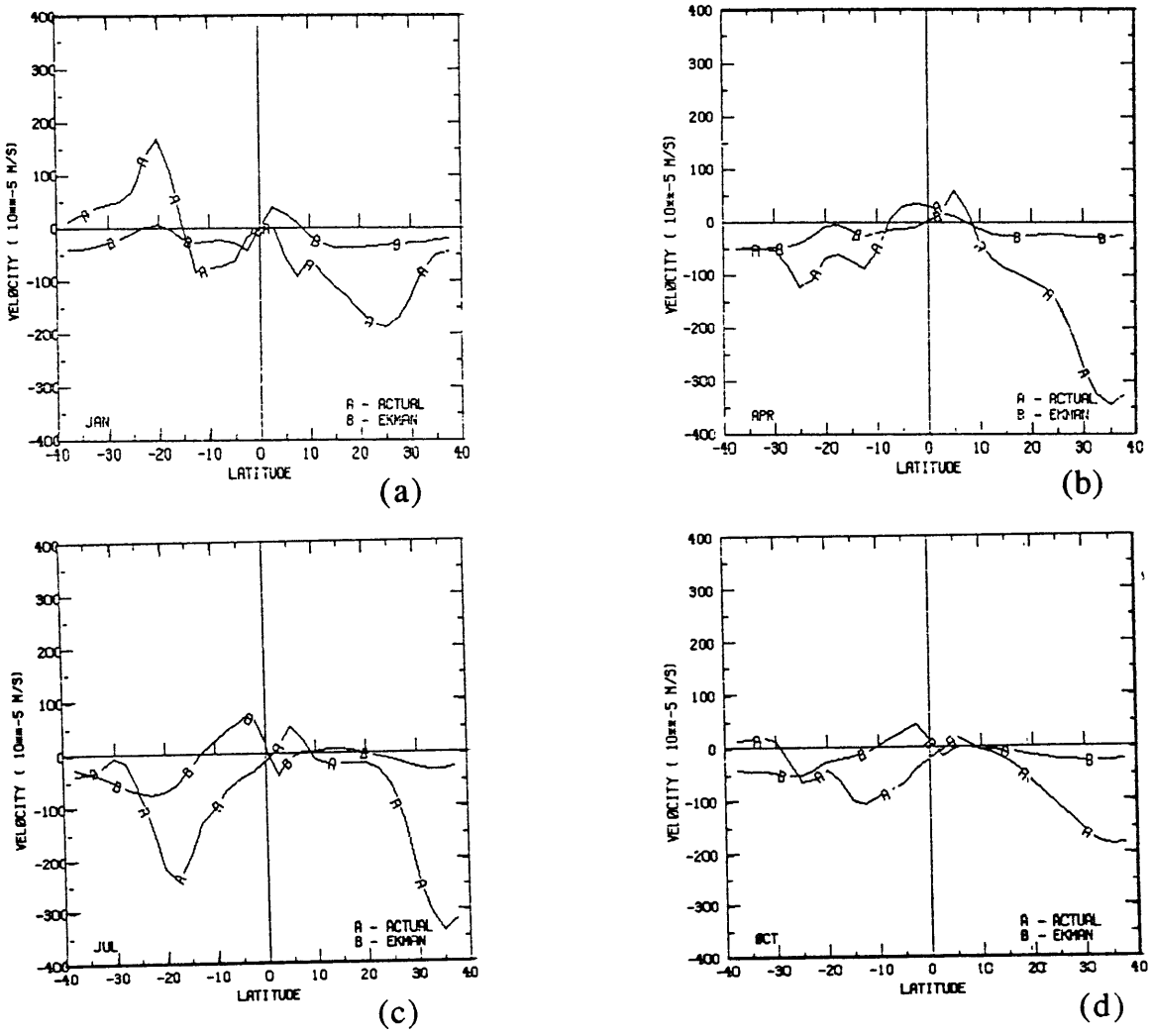

Figure 4.6 Identical to figure 4.4 except for region III.

a notable feature of the plots is the westward increase in magnitude of the Ekman velocities near the equator. This feature is a reflection of the westward increase of the vorticity magnitudes. To a lesser degree, the same thing is true for the actual vertical velocities. Another notable feature is the westward increase of meridional symmetry of the Ekman velocity for the months of July and October. The profiles for w_E in region I for these months are in fact, almost perfectly symmetric about the equator to about 10-15 degrees on either side, with peaks near 5S and 10N, while the actual vertical velocity profiles for these same graphs, although comparably symmetric, show only a single-peak structure. The smaller magnitudes of the calculated Ekman velocities at higher latitudes could be due to the use of a constant K. Calculations of Ekman velocities using the 2-D model data indicated higher values of K farther from the equator. The higher values would enhance the magnitudes of the calculated Ekman velocities at these latitudes.

As an overall observation, qualitative agreement is quite good between the two vertical velocity fields poleward of 15°. This is indicated by the locations of the Ekman velocity maxima relative to those obtained from integration of Eq. (24) and also by the correlation between westwardly increasing magnitudes of vorticity maxima to westwardly increasing magnitudes of vertical velocity maxima obtained through integration of Eq. (24). Within the region of 15S to 15N, however, qualitative agreement seems limited only to July and October for region I. This disagreement may again be attributable to the inaccuracies of meridional velocity data within

the region.

4.5 Meridional Temperature Gradients

The third assumption of the theory to be investigated was that the meridional temperature gradient at the top of the PBL is equal to that at the surface. Here, the meridional temperature gradients at 950 mb and 850 mb are compared to the meridional SST gradient below, for the various regions. The 850 mb and 950 mb levels are shown because generally, they correspond to the two levels above and below the LCL. Thus, verification of the assumption that the the meridional temperature gradient at both levels equals the SST gradient implies verification at the LCL. The results for the meridional temperature gradient calculations are graphically summarized in figures 4.7 and 4.8. The vertical axis is temperature gradient in units of 10^{-6} K/m and the horizontal axis is latitude, with negative numbers indicating the southern hemisphere. The results are plotted from 37.5S to 37.5N.

Figure 4.7 shows the results for all three regions for the transition months (April and October). Upon initial inspection, it can be seen that agreement between the gradients at the surface and those at lower levels is not as good as the agreement found with the 2-D model data set. The quasi-linearity of the SST gradients does, however, correlate with that of the meridional temperature gradients at the lower levels, quite well. This is particularly true in those areas where the nonlinearity of the SST gradients is small in both size and scale.

Figure 4.8 is identical in format to figure 4.7, except the

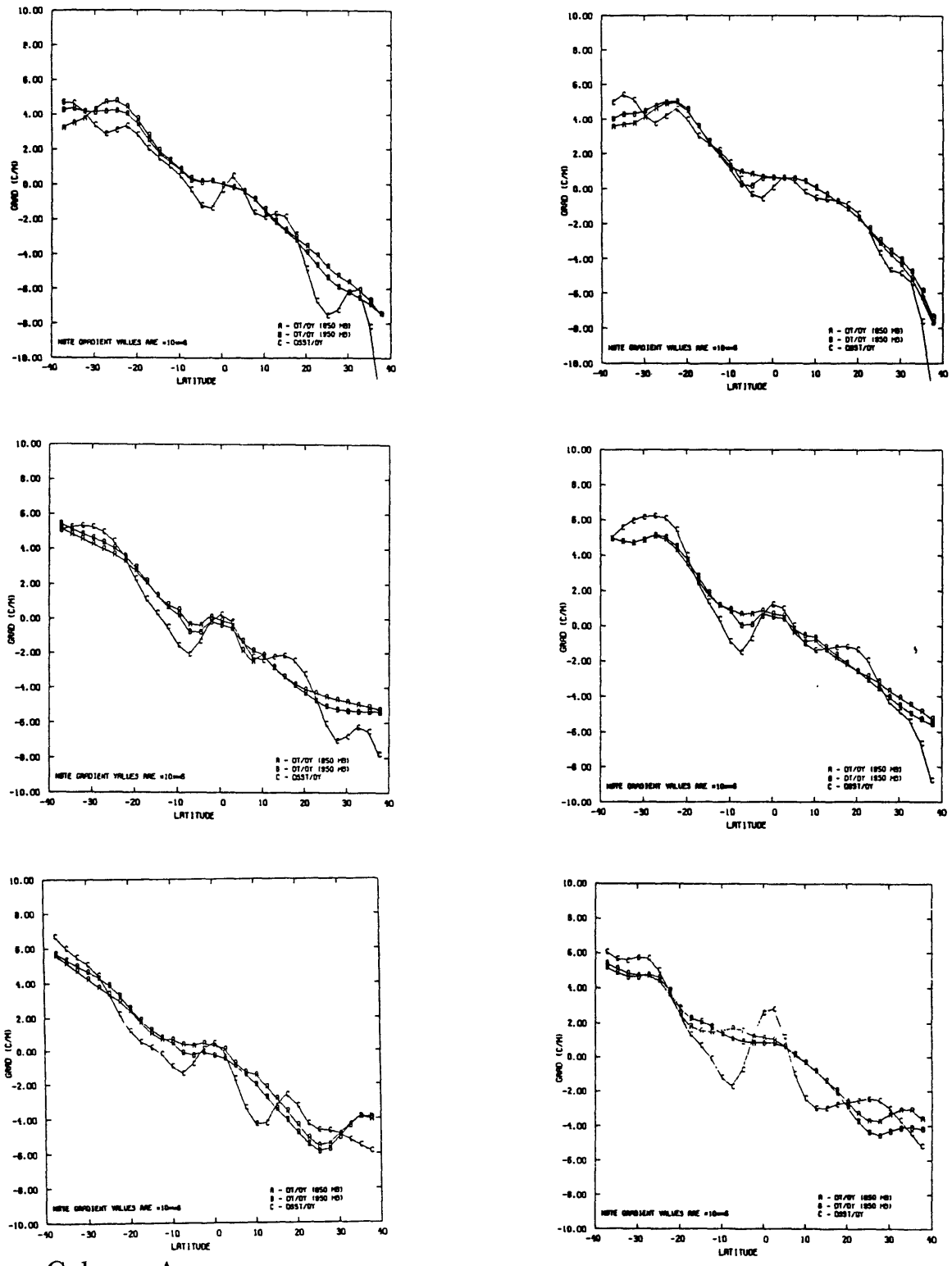

Column A

Column B

Figure 4.7 Meridional temperature gradients at 850 mb (A), 950 mb (B), and at the surface (C) for region I (upper), region II (middle), and region III (lower) for April (column A) and October (column B). Note gradient values are $x10^{-6}$ $^{o}C/m$.

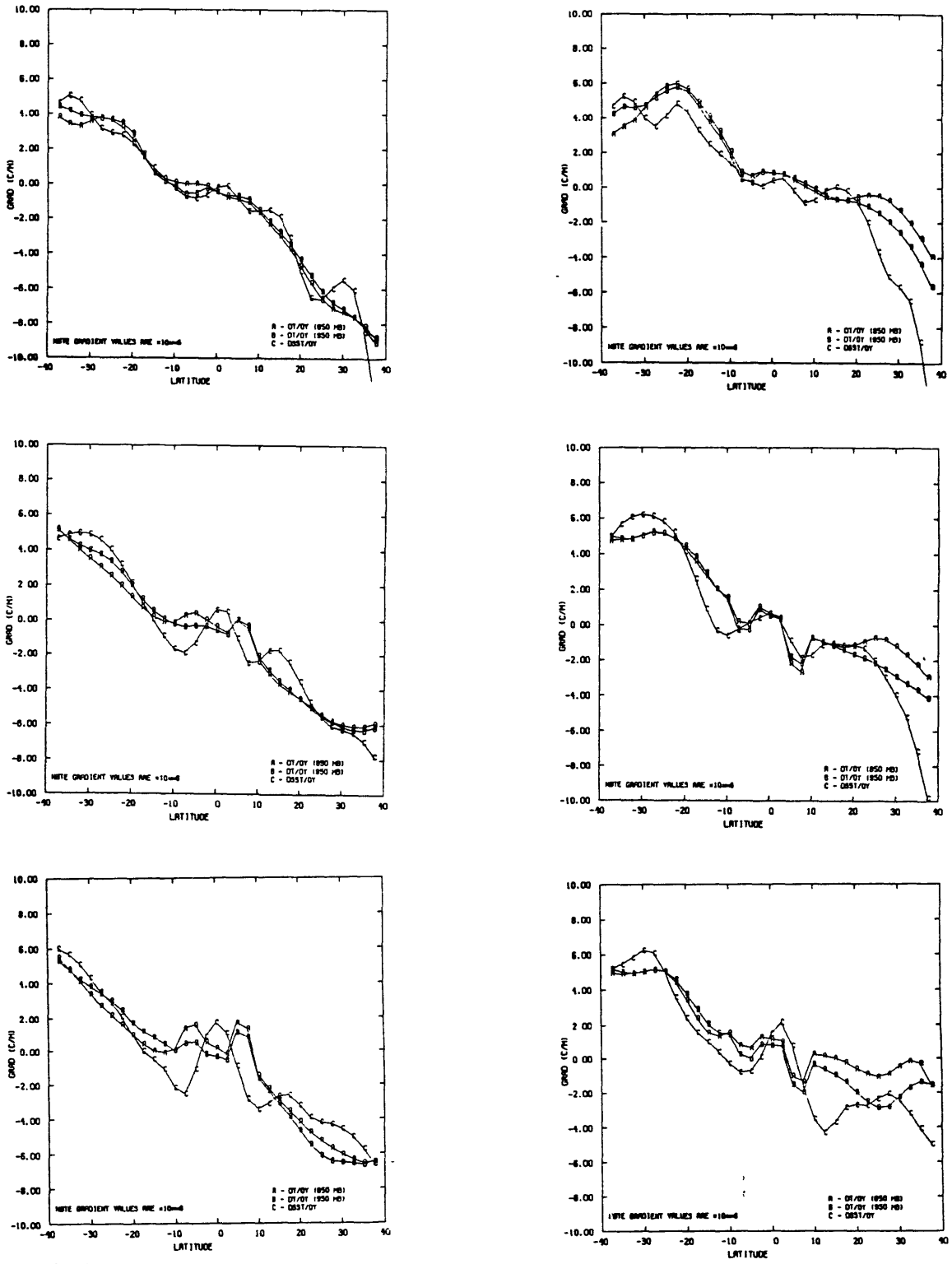

Column A

Column B

Figure 4.8 Identical to figure 4.10 except for January (column A) and July (column B).

results for the months of January and July for the three regions are shown. For these two months, agreement is slightly worse at higher latitudes and also in tropical latitudes, wherever meridional gradients in the SST are nonlinear and large.

Overall however, the assumption that the meridional temperature gradient at the top of the PBL is equal to that at the surface, seems a valid one for all three regions and particularly during the months of April and October. Again, this is not surprising and in fact it can be easily shown that to first order, the meridional temperature gradient at the top of the PBL is proportional to that at the surface, dropping off vertically as $(P_{PBT}/P_{SFC})^{R/C_P}$. Hence, the attenuation increases slowly with height. Similar results were also obtained using the 2-D model data and other studies using different 3-D data sets have shown positive correlations between surface and low-level temperature gradients as high up as 700 mb (Nigam and Lindzen, 1986).

4.6 Theoretical Vorticity

Before verification of the vorticity prediction could be assessed accurately, a rough estimate of the valid sub regions was needed. This included determining (1) the location of the ascent regions and also (2) the location of areas poleward of S^* maxima. The ascent region boundaries were determined using the vertical velocity profiles obtained through integration of the continuity equation. Since these vertical velocities were only for the 900 mb level, in order to determine the ascent region boundaries, it was assumed that their locations throughout the troposphere did not

deviate vertically from those at 900 mb. This was not a bad assumption since it was observed to be very nearly the case with the 2-D model data. Also, since the 2-D theory is constrained to a meridionally symmetric S^* distribution, really only those ascent regions which encompass an S^* maximum at the equator are relevant for examination. More generally however, it is reasonable to assume that any ascent region poleward of an S^* maximum is also a valid region. This is feasible since once again there are no theoretical constraints coupling the dynamics and thermodynamics equatorward of the latitude in question to the vorticity at that latitude. The list of valid subregions is specified in table 4.1.

Calculations of du/dy using equation (15) were done for all three regions and for all four months in the valid subregions specified in Table 4.1. The method of calculation was identical to that used in the 2-D model analysis. The results, however, showed the values of du/dy to be constant for a given latitude as a function of y_0. Closer inspection revealed the reason for this to be the domination of the βy term over the dS^*/dy term by one to two orders of magnitude. Thus, even those cases where the calculated values for du/dy were close to the actual values were considered to be purely coincidental.

In order for the dS^*/dy term to be larger, either dS^*/dy itself would have to be larger at the top of the PBL, or outflow temperatures would have to be colder. In order for outflow temperatures to be colder, the isentropes would have to be less flared, i.e. the two fields would have to be more congruent. This may be an indication that S^* also is not conserved by ascending

REGION	JANUARY	APRIL	JULY	OCTOBER
I (175E to 155E)	14S to 9N	16S to 10N	15S to 12N	13S to 19N
II (145W to 175W)	37S to 5S	33S to 8S	3N to 8N	22S to 11S
III (125W to 145W)	37S to 15S	8S to 8N	2N to 8N	3N to 8N

Table 4.1 The subregions within each region relevant for examination of prediction (1) are shown for each of the four months.

parcels.

4.7 Vertical Velocity and Sea Surface Temperature

The vertical velocity prediction of the theory was investigated despite the fact that neither the assumption that $S^* = S^*(M)$ nor the vorticity prediction was valid in any of the regions. This was done to determine how sensitive the verification of this prediction was to the validity of the assumptions. Figures 4.9 - 4.11 are the 3-D counterparts to figure 3.16 showing the vertical velocity profiles at 900 mb obtained through integration of Eq. (24) and also the corresponding SST distributions for all the regions and the four months. Examination of the results for the four months for each region separately is helpful to observe possible correlations in the annual cycles of both SST distributions and vertical velocities. Verification of this prediction may thus be more easily assessed.

Figure 4.9 (region I) shows that the location of the maximum in SST has a very small annual cycle. The SST distribution never has a single, well defined peak at any time and meridional SST gradients between peaks are very small. The magnitudes of the meridional SST gradients poleward of the SST maxima either remain constant or slowly increase away from the equator. A single broad region of ascent is present during January and October, a weak double maximum is present during April, and a very distinct double maximum is present during July. Maximum SST's are near 29° C during all months.

Figure 4.10 (region II) shows an even more prominent double peak structure for the SST distribution. The annual cycle in

SST at low latitudes is also more noticeable. Both the amplitude of the annual migration of the SST maximum as well as the amplitude of the annual SST variation at a given location are larger than in region I. The corresponding vertical velocity profiles indicate strong ascent (~ 200 x 10^{-5} m/s) centered near 20S during January and much weaker ascent during the other three months. The amplitude of the annual migration (from January to July) of the position of maximum ascent is much larger in this region (~22.5°) than in region I. The mean position of ascent changes rapidly from April to July and from July to October while the change in position of the SST maximum is more constant throughout the year.

Figure 4.11 (region III) again shows a well defined annual SST variation in both the amplitude of annual migration of SST maximum as well as the amplitude of annual SST variation at a given location. The annual migration in position of SST maximum is very pronounced with the most rapid migration occurring from April to July and from October to January. The vertical velocity profile again shows a well defined single maximum in January near 20S and much smaller magnitudes for the other three months. The mean position of ascent changes most rapidly from January to April and from October to January.

In summary, figures 4.9 - 4.11 indicate westwardly increasing meridional symmetry in both SST and vertical velocity profiles for all months. Magnitudes of SST and vertical velocity maxima also increase westward in an annual mean sense, while magnitudes of meridional SST gradients do not. Hence, the vertical

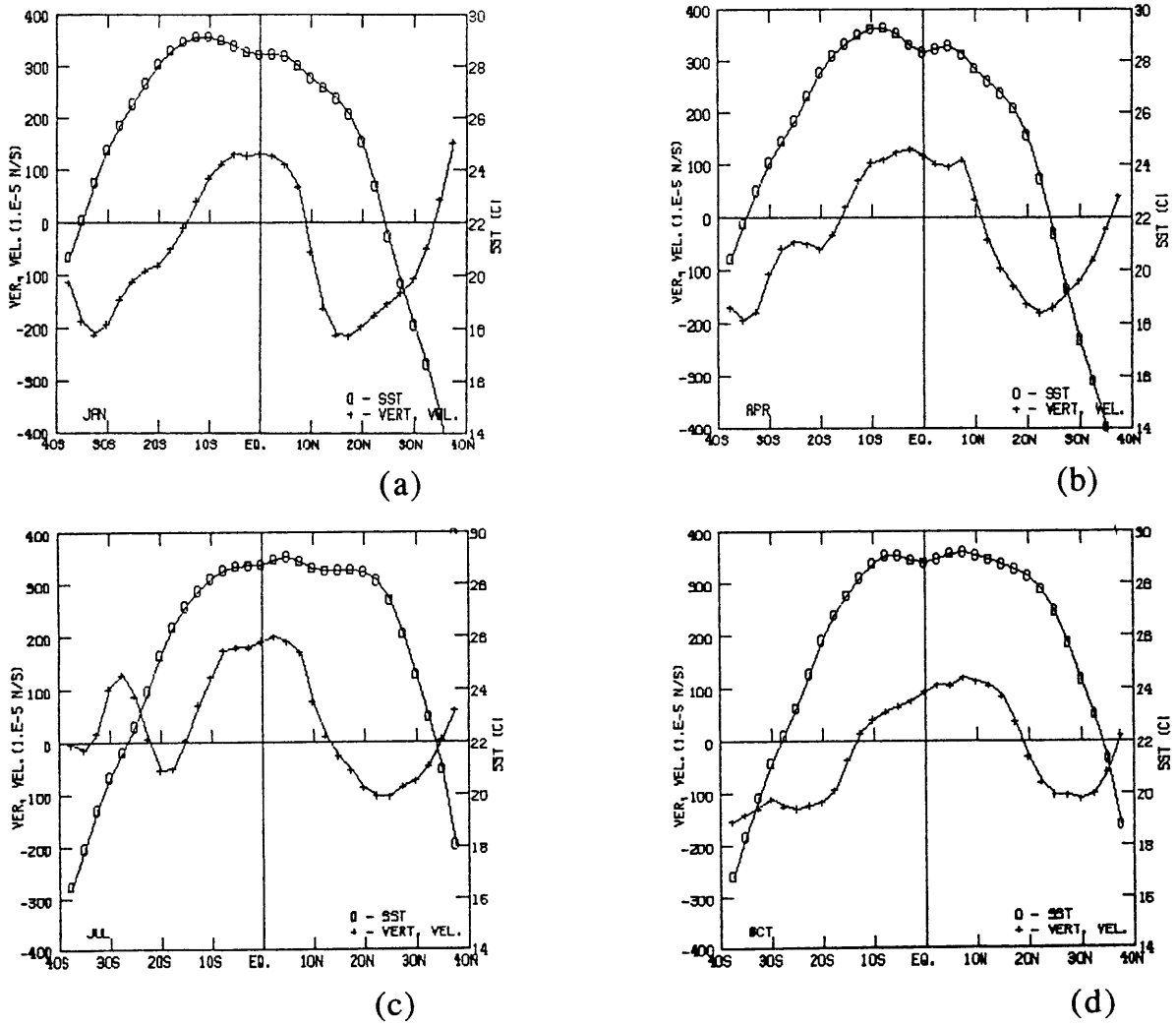

Figure 4.9 Actual vertical velocities (+) at 900 mb obtained from integration of Eq. (24) and sea surface temperatures (0) for region I for (a) January, (b) April, (c) July, and (d) October.

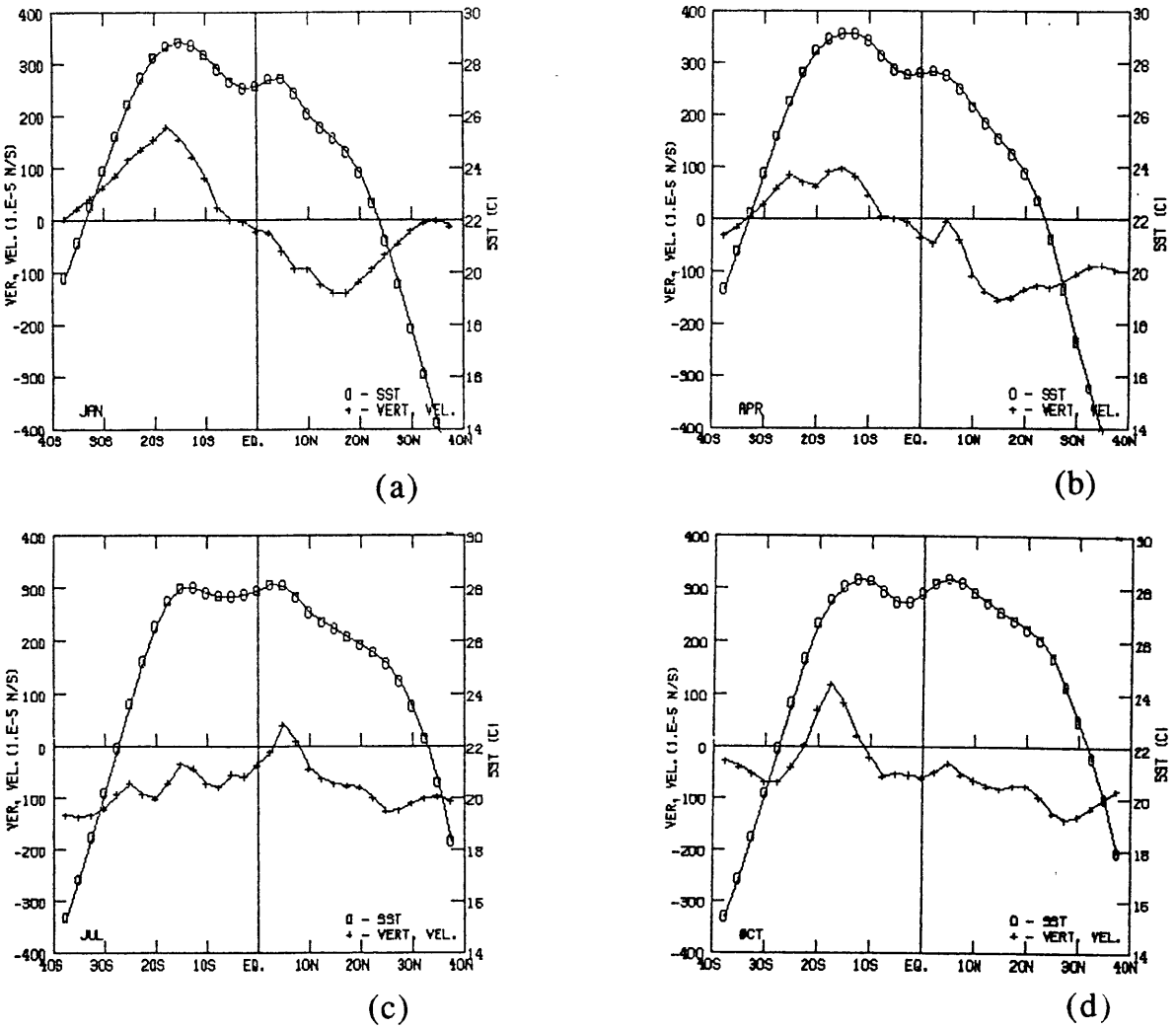

Figure 4.10 Identical to figure 4.9 except for region II.

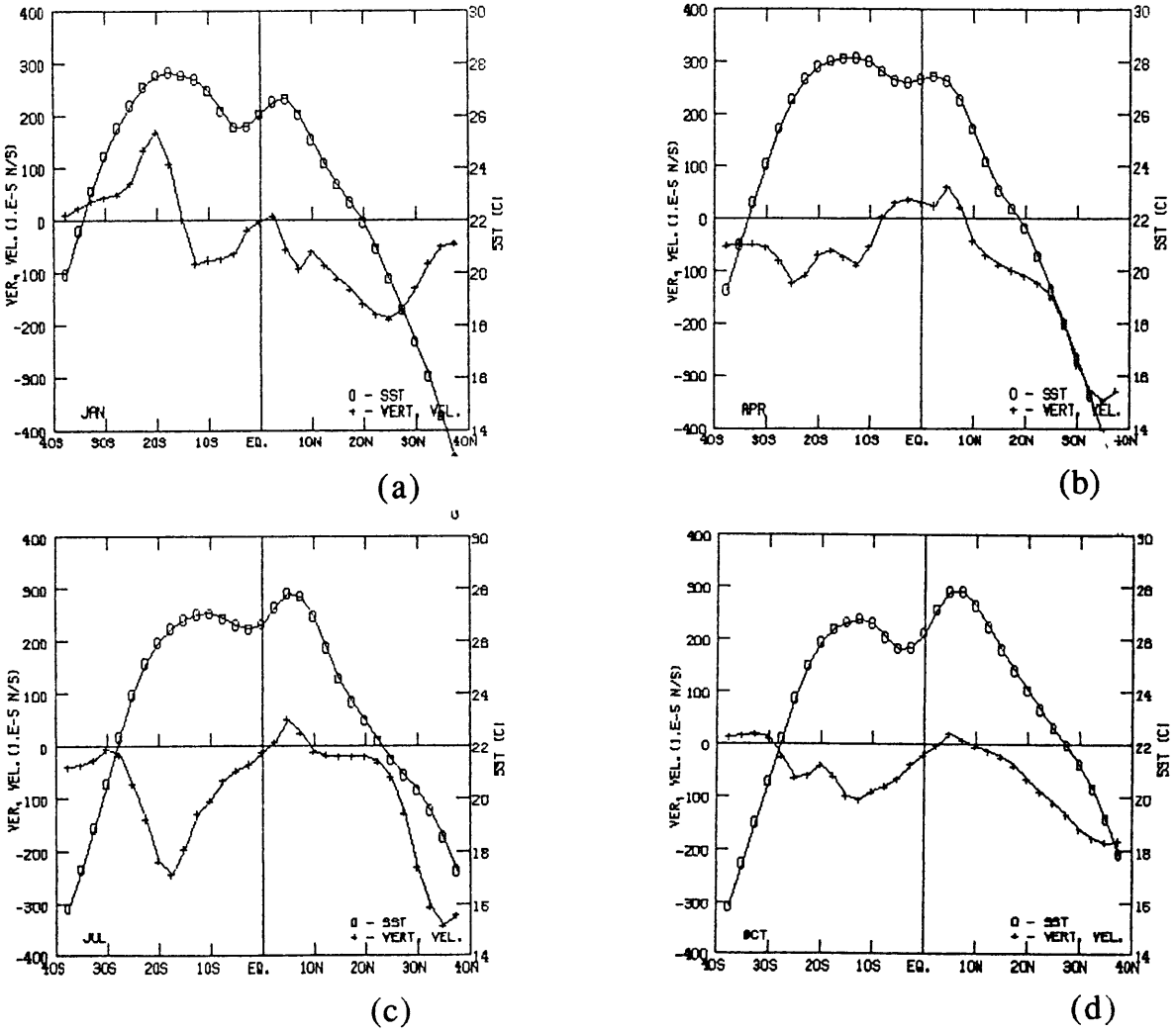

Figure 4.11 Identical to figure 4.9 except for region III.

velocity prediction is not verified in any of the regions with this data set.

CHAPTER V
SUMMARY AND CONCLUSIONS

A two dimensional theory to explain the vertical motions at the top of the PBL was presented. The assumptions and predictions of the theory were investigated using data sets from a 2-D GCM and actual 3-D data as well. The 2-D GCM data sets were examined to qualitatively determine the degree of validity required by each of the assumptions in order for the predictions to be verified. The 3-D data set was investigated to determine if any region existed where the theory could be used to predict the vertical motions at the top of the PBL.

Results from the 2-D model data analyses showed that assumption (1), stating that S^* and M are conserved quantities of ascending parcels, proved to be valid in three of the six runs: NC1-A, NC1-S1, and MC2-A. The quantity M was conserved in those runs which either excluded momentum mixing or had relatively intense meridional circulations. The quantity S^* was conserved in those runs which had relatively weak meridional circulations. Hence, assumption (1) proved to be valid only in those runs which satisfied conditions (to some degree) for both quantities to be conserved. These results can be explained from the standpoint that in the model's momentum mixing scheme, environmental wind shear has less time to act on parcels ascending rapidly in cumulus towers than on parcels ascending slowly. Hence, removal of this parameterization or existence of strong ascent will result in ascending parcels more likely to conserve M. The degree of

convective mixing of S^* is, in contrast, dependent on the vertical ascent rate. Hence, more slowly ascending parcels will mix less with the environment and conserve their S* to a higher degree.

Assumption (2), stating that the vertical velocity at the top of the PBL can be estimated by Ekman pumping theory, proved to be valid in only three of the six runs: MC2-A, MD-A, and MC1-A. The assumption was not a good one in those runs which excluded momentum mixing or in those with meridionally symmetric SST distributions. The violation of this assumption by the runs with symmetric SST distributions is somewhat puzzling but perhaps may be attributable to the fact that the steady state model vertical velocity profiles for these runs were somewhat noisy. This idea is supported by the fact that for the two 'meridionally symmetric' runs (NC1-S1 and NC1-S2), the vorticity patterns at 854 mb are similar (and meridionally symmetric) to each other while the vertical velocity profiles at 854 mb are neither similar nor meridionally symmetric to each other.

Assumption (3), stating that the meridional temperature gradient at the top of the PBL is equal to that at the surface, proved to be valid in all runs. The validity of this assumption was not dependent on sea surface temperature distribution although slightly better agreement between surface and low level meridional temperature gradients was evident in those runs with sinusoidal SST distributions. This, however, was likely a consequence of the smoothing scheme used on the temperature field.

Qualitative verification of Eq. (15), the vorticity prediction,

by the same runs for which assumption (1) was valid indicates the importance of that assumption being valid to at least some degree. Calculation of du/dy as a function of y_0 indicated no exceptional behavior in the graphs at y_0, the optimally chosen value for y_0, although poleward of this latitude the calculated values for du/dy were much more random as a function of y_0 than equatorward of this latitude.

The verification of prediction (2) was examined separately from that of prediction (1) to determine in each run, the validity of this prediction independent of the validity of the assumptions. Verification was difficult to assess despite the presence of a double ITCZ straddling an SST maximum in three of the six runs: MC2-A, MC1-A, and NC1-A. The difficulty arises because the magnitude of the meridional SST gradient increases away from the equator. Hence, from the locations of the ascent regions in these three runs, assessment of verification of prediction (2) was difficult.

The results for the three assumptions and two predictions for each run are summarized in Table 5.1. The headings A1 - A3, P1, and P2 refer to the three assumptions and two predictions respectively. A shaded box indicates either that the assumption was valid or the prediction was verified. The criteria used to determine whether a particular box should be shaded was that the assumption or prediction had to be detectably valid in some region of that run. Note that for P2, the abovementioned three runs are shaded since there is no evidence that the prediction was not verified.

For the 3-D data set, assumption (1) did not prove to be

valid in any of the selected regions during any of the months. Lack of sufficient data hindered determination of the exact causes for this although the increased lack of congruity between S^* and M from summer to winter hemispheres may indicate that M and S^* are not conserved to varying degrees throughout the year. This can be concluded if the conservation dependence of each quantity on ascent rate is similar to that deduced from the 2-D model data analyses. A more intense large-scale ascent present in winter hemispheres would result in M being more conserved and S^* being less conserved. Hence, the two fields would appear more congruent.

Assumption (2) proved to be valid in regions I, II, and III poleward of 15° N and 15° S. Within this band, the assumption appeared valid only for region I during July and October. Inaccuracies in the meridional wind data (and hence inaccurate determination of vertical velocities) result in inconclusive evidence about the validity of assumption (2) in this narrow band. The smaller velocities calculated from Ekman pumping theory may be attributable to the use of a constant eddy viscosity coefficient although this did not affect the locations of ascent and descent.

Assumption (3) proved to be valid for all the selected regions and months. This was particularly evident where nonlinear meridional SST gradients were large in spatial scale and small in amplitude, i.e. where the meridional temperature gradient profiles at low levels were much smoother.

Neither of the predictions was verified with the 3-D data set in any of the selected regions. For prediction (1), the vorticity pattern at the top of the PBL could not be approximated using Eq.

(15). The reason for this is thought to be the violation of assumption (1). Prediction (2) was not considered verified since the majority of cases examined indicated single ITCZ structures whose locations were seemingly independent of either the locations or the magnitudes of meridional SST gradients. The reason for this is again thought to be the violation of assumption (1), which states that S^* and M are conserved quantities of ascending parcels. It should be noted that in cases where lines of constant S^* are purely vertical, (i.e. no "flare") it can be shown that the pressure distribution and hence the vorticity pattern at the top of the PBL will to first order, be proportional to d^2T_{PBT}/dy^2, where T_{PBT} is the temperature at the top of the PBL. In the 3-D cases examined, it is thus hypothesized that the vorticity and vertical velocity profiles at the top of the PBL can be explained as a composite of those predicted by the presently investigated theory and those due to purely vertical lines of constant S^*.

In conclusion, it has been shown that the validity of assumption (1) is a requirement for the verification of prediction (1). Qualitative verification can be observed, however, if S^* and M are only partially congruent; i.e. if along a line of constant S^*, $(dS^*/dM)_P$ at the top of the PBL and $(dS^*/dM)_y$ in the troposphere are within a factor of two of each other. The vertical velocity profile at the top of the PBL can be reasonably approximated using Ekman pumping theory. Prediction (2) can not be verified quite so well, even exclusively from prediction (1) except in run MC2-A. Although it was not shown explicitly, validity of all three assumptions and verification of prediction (1) implies the

verification of prediction (2) with values of du/dy calculated from Eq. (15). Assumption (3) is a valid assumption for all runs and regions examined. Finally, it is concluded that the non-conservation of M and possibly S^* are important considerations when formulating theories about the Hadley Circulation.

RUN	A1	A2	A3	P1	P2
NC1-S1					
NC1-S2					
MC2-A					
MD-A					
MC1-A					
NC1-A					

Table 5.1 The 2-D model data analyses are summarized. Headings A1-A3, P1, and P3 refer to the three assumptions and two predictions which were examined. Shading indicates validity or verification to a detectable degree.

ILLUSTRATION LIST

Figures

Figure 2.1 (a) contour plot showing lines of constant S^*. Streamlines and constant M lines are parallel to these. Spacing indicates weak baroclinity at streamlines a and c and strong baroclinity at streamline b. (b) Similar to (a) except for presence ofβ and constant spacing of contour intervals of S^*.

Figure 3.1 Latitude-pressure contour plots of streamfunction (solid (>0) and dashed (<0) lines, interval is 10^9 kg/s) and absolute angular momentum (dotted lines, interval is 10 m^2/s) for the six 2-D model runs: (a) NC1-S1, (b) NC1-S2, (c) MC2-A, (d) MD-A, (e) MC1-A, and (f) NC1-A.

Figure 3.2 Latitude-pressure contour plots of saturated moist entropy (solid lines, interval is 10 J/kgK) with LCL = 959 mb and M (dotted (interval is 10 m/s) and dashed (interval is 4 m/s) lines) for the six 2-D model runs: (a) NC1-S1, (b) NC1-S2, (c) MC2-A, (d) MD-A, (e) MC1-A, and (f) NC1-A.

Figure 3.3 Identical to figure 3.2 except for LCL = 894 mb.

Figure 3.4 Latitude-pressure contour plots of streamfunction (solid (>0) and dashed (<0) lines, interval is 10^9 kg/s) and saturated moist entropy (dotted lines, interval is 10 J/kgK) for the six 2-D model runs: (a) NC1-S1, (b) NC1-S2, (c) MC2-A, (d) MD-A, (e) MC1-A, and (f) NC1-A.

Figure 3.5 Profiles of dM/dS* (+) calculated in the y-direction and S* (*) at 934 mb for the six 2-D model runs: (a) NC1-S1, (b) NC1-S2, (c) MC2-A, (d) MD-A, (e) MC1-A, and (f) NC1-A.

Figure 3.6 Latitude-pressure contour plots of dM/dS^* calculated in the P-direction (column A) and in the y-direction (column B) for runs NC1-S1 (top), NC1-S2 (middle), and MC2-A (bottom). Shading indicates values between 1.0 and 2.0 $^oC/(m/s)$

Figure 3.6 (cont'd) Runs MD-A (top), MC1-A (middle), and NC1-A (bottom).

Figure 3.7 Ekman vertical velocities (A) calculated at 894 mb and model vertical velocities (B) at 854 mb for the six 2-D model runs: (a) NC1-S1, (b) NC1-S2, (c) MC2-A, (d) MD-A, (e) MC1-A, and (f) NC1-A.

Figure 3.8 Meridional temperature gradients at 894 mb (A), 959 mb (B), and at the surface (C) for the six 2-D model runs: (a) NC1-S1, (b) NC1-S2, (c) MC2-A, (d) MD-A, (e) MC1-A, and (f) NC1-A.

Figure 3.9 Ratio of theoretically calculated du/dy to numerical

value of du/dy as a function of y_0 for run NC1-S1 (leftmost column) and run NC1-S2 (three rightmost columns). Dagger indicates optimum choice of y_0. The latitude and pressure of the calculation, as well as the numerical value of du/dy are listed under each plot.

Figure 3.10 Identical to figure 3.9 except for run MC2-A.

Figure 3.11 Identical to figure 3.9 except for run MC2-A (cont'd).

Figure 3.12 Identical to figure 3.9 except for run MD-A.

Figure 3.13 Identical to figure 3.9 except for run MC1-A.

Figure 3.14 Identical to figure 3.9 except for run MC1-A (cont'd).

Figure 3.15 Identical to figure 3.9 except for run NC1-A.

Figure 3.16 Model vertical velocities (+) at 854 mb and sea surface temperatures (0) for the six 2-D model runs: (a) NC1-S1, (b) NC1-S2, (c) MC2-A, (d) MD-A, (e) MC1-A, and (f) NC1-A.

Figure 4.1 Latitude-pressure contour plots of saturated moist entropy (solid lines, interval is 10 J/kgK) with LCL = 900 mb and M (dotted (contour interval is 10 m^2/s) and dashed (contour interval is 4 m^2/s) lines) for region I (upper), region II (middle), and region III (lower) for April (column A) and October (column B).

Figure 4.2 Identical to figure 4.1 except for January (column A) and July (column B).

Figure 4.3 Profiles of dM/dS^* (*) calculated in the y-direction at 900 mb and latitude-pressure contour plots of dM/dS^* calculated in the P-direction for region I (upper), region II (middle), and region III (lower) for April (column A) and October (column B). Shading indicates values between 1.0 and 2.0 $^oC/(m/s)$.

Figure 4.4 Calculated Ekman vertical velocities at 900 mb (B) and actual vertical velocities (A) obtained from integration of Eq. (24) for region I for (a) January, (b) April, (c) July, and (d) October.

Figure 4.5 Identical to figure 4.4 except for region II.

Figure 4.6 Identical to figure 4.4 except for region III.

Figure 4.7 Meridional temperature gradients at 850 mb (A), 950 mb (B), and at the surface (C) for region I (upper), region II (middle), and region III (lower) for April (column A) and October (column B). Note gradient values are $x10^{-6}$ $^oC/m$.

Figure 4.8 Identical to figure 4.7 except for January (column A) and July (column B).

Figure 4.9 Actual vertical velocities (+) at 900 mb obtained from integration of Eq. (24) and sea surface temperatures (0) for region

I for (a) January, (b) April, (c) July, and (d) October.

Figure 4.10 Identical to figure 4.9 except for region II.

Figure 4.11 Identical to figure 4.9 except for region III.

Tables

Table 3.1 The differences among the runs with respect to moist convection parameterizations, large-scale zonal eddy forcing, vertical momentum mixing, and meridionally symmetric sea surface temperature distributions are shown.

Table 4.1 The subregions within each region relevant for examination of prediction (1) are shown for each of the four months.

Table 5.1 The 2-D model data analyses are summarized. Headings A1-A3, P1, and P3 refer to the three assumptions and two predictions which were examined. Shading indicates validity or verification to a detectable degree.

REFERENCES

Albrecht, B. A., 1984: A model study of downstream variations of the thermodynamic structure of the trade winds. *Tellus* , **36A**, 187-202.

Arakawa, Akio and W. H. Schubert, 1974: Interaction of a cumulus cloud ensemble with the large scale environment, Part I. *J. Atmos. Sci.* , **31**, 674-701.

Chervin, R. M. and L. M. Druyan, 1984: The influence of ocean surface temperature gradient and continentality on the Walker Circulation. Part I: prescribed tropical changes. *Mon. Wea. Rev.* , **112**, 1510-1523.

Goswami, B. N. , J. Shukla, E. K. Schneider, and Y.C. Sud, 1984: Study of the dynamics of the intertropical convergence zone with a symmetric version of the GLAS climate model. *J. Atmos. Sci.* , **41**, 5-19.

Hansen, J., G. Russell, D. Rind, P. Stone, A. Lacis, S. Lebedeff, R. Ruedy, and L. Travis, 1983: Efficient three dimensional global models for climate studies: models I and II. *Mon. Wea. Rev.* , **111**, 609-662.

Helfand, H. M., 1979: The effect of cumulus friction on the simulation of the January Hadley Circulation by the GLAS model of the general circulation. *J. Atmos. Sci.* , **36**, 1827-1843.

Horel, J. D., 1982: On the annual cycle of the tropical Pacific Atmosphere and Ocean. *Mon. Wea. Rev.* , **110**, 1863-1878.

Nigam, S. and R. S. Lindzen, 1986: On the role of sea surface temperature gradients in forcing low level winds and convergence in the tropics. Unpublished.

Oort, A. H., 1983: *Global Atmospheric Circulation Statistics, 1958-1973* . NOAA professional paper 14, Geophysical Fluid Dynamics Laboratory, Princeton, NJ, 180 pp.

Rind, D. and W. B. Rossow, 1984: The effects of physical processes on the Hadley Circulation. *J. Atmos. Sci.* , **41**, 479-507.

Rogers, R. R., 1979: A Short Course in Cloud Physics, 2nd ed., Pergamon Press, 235 pp.

Schneider, E. K. and R. S. Lindzen, 1976: A discussion of the parameterization of momentum exchange by cumulus convection. *J. Geoph. Res.* , **81**, 3158-3160.

Yao, Mao-Sung and P. H. Stone, 1987: Development of a two dimensional zonally averaged statistical dynamical model. Part I: the parameterization of moist convection and its role in the general circulation. *J. Atmos. Sci.* , in press.